EFFECTS OF LATERAL SPREADING ON PILE FOUNDATIONS
Data report on tests SKH-13-17

S.K. Haigh[1]

CUED/D-SOILS/TR318 (2002)

[1] Research Associate, Cambridge University Engineering Department

Table of Contents

List of Figures

List of Tables

1. Introduction

The many large earthquakes of recent years, including those at Northridge (1994), Kobe (1995), Turkey (1999), Taiwan (1999) and Gujarat (2001) have shown the capacity of these large-magnitude events to cause massive damage to infrastructure and enormous loss of life. The concentrations of population in seismically active regions of the world, including the Pacific Rim, California and northern India has put many millions of people at risk when these large earthquakes strike. Whilst nothing can be done to prevent these earthquakes from occurring, efforts must be made to find ways to minimise the impact of these earthquakes on the population and infrastructure.

In many of these major earthquakes, large-scale damage due to liquefaction and especially due to the lateral spreading of liquefiable slopes has been observed. In the Niigata Earthquake of 1964, lateral spreading of up to 5 m was observed along the Shinano River (Hamada 1992). These large magnitude deformations have been shown to have devastating effects on structures founded on these slopes and lifelines passing over or through them. In particular, pile foundations passing through these deposits have been shown to be at risk from the lateral loads exerted on them by the flowing deposits. One example of this investigated by Hamada was the collapse of the Showa bridge in Niigata, as shown in Figure 1. It can be seen that the loads imposed on the piles by the laterally spreading soil was sufficient to cause the pier heads to deflect by approximately 1 m and the bridge decks to fall from their bearings.

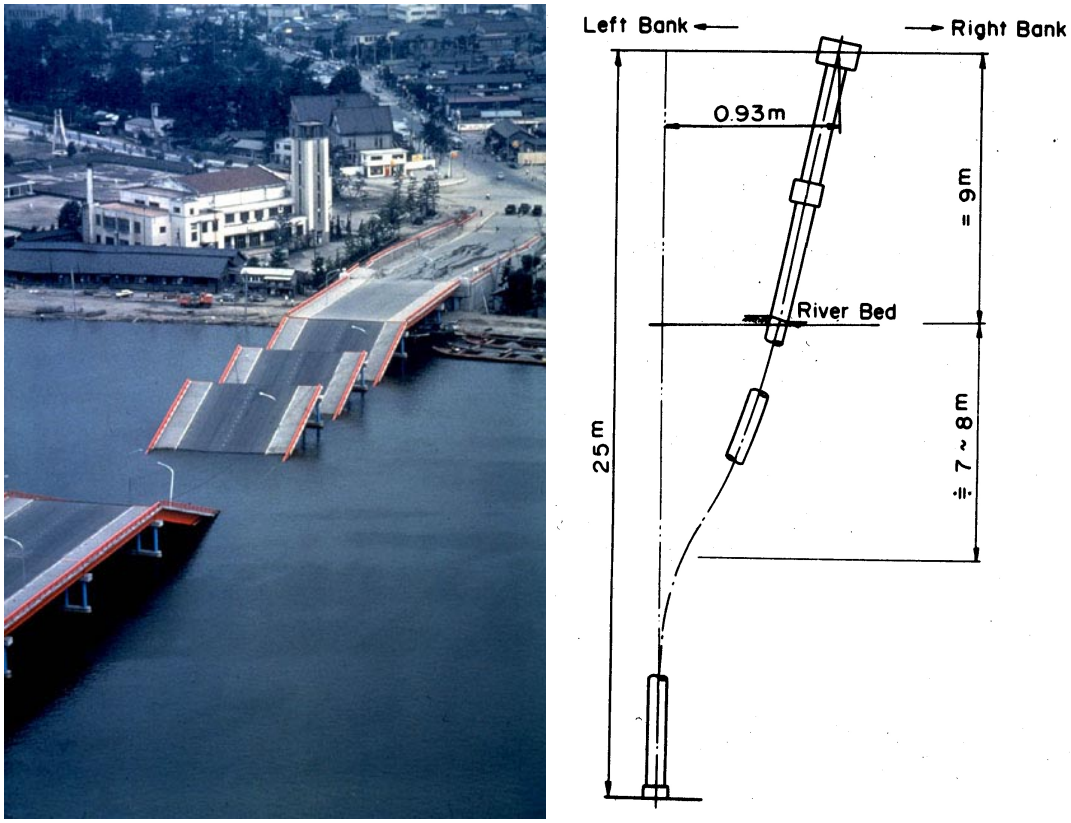

Figure 1: Collapse of the Showa Bridge and one of its piles.

The lateral loads applied by these flowing slopes can hence be seen to be very important to the performance of structures resting on piles passing through sloping liquefiable deposits.

This research was hence undertaken to investigate the interaction of these spreading slopes with pile foundations. The research consisted of a series of five beam centrifuge tests (SKH-13 to 17). Full details of the analysis of these test results is given by Haigh (2002).

2. Experimental Procedure

The test series consisted of five oil-saturated tests (SKH-13 to 17). The models were all prepared and tested following the procedure outlined in the next section.

2.1 Model Preparation

All tests from SKH-13 through to SKH-17 comprised of slopes of loose liquefiable fraction E silica sand with properties as shown in Table 1 and particle size distribution as shown in Figure 1. The models were prepared to a nominal void ratio of 0.8 or an R_D (relative density) of 50% by air pluviation from an overhead hopper. Density was controlled by adjusting both the height of the hopper and the rate of pouring. End reservoirs of Fraction B silica sand, with properties as shown in Table 2 and particle size distribution as shown in Figure 1, were provided at the top and bottom of the slope to ensure a plane strain seepage condition through the model. These are separated from the rest of the sand by stainless steel mesh and are filled at the same rate as the rest of the model.

Table 1: Properties of fraction E silica sand. (after Tan, 1990)

Property	Value
ϕ_{crit}	32^0
D_{10}	0.095 mm
D_{50}	0.14 mm
D_{60}	0.15 mm
e_{min}	0.613
e_{max}	1.014
k with water at e = 0.72	0.98E-04 m/s
G_s	2.65

Table 2: Properties of fraction B silica sand. (after Lee, 1990)

Property	Value
ϕ_{crit}	36^0
D_{10}	0.84 mm
D_{50}	0.9 mm
D_{90}	1.07 mm
e_{min}	0.495
e_{max}	0.82
G_s	2.65

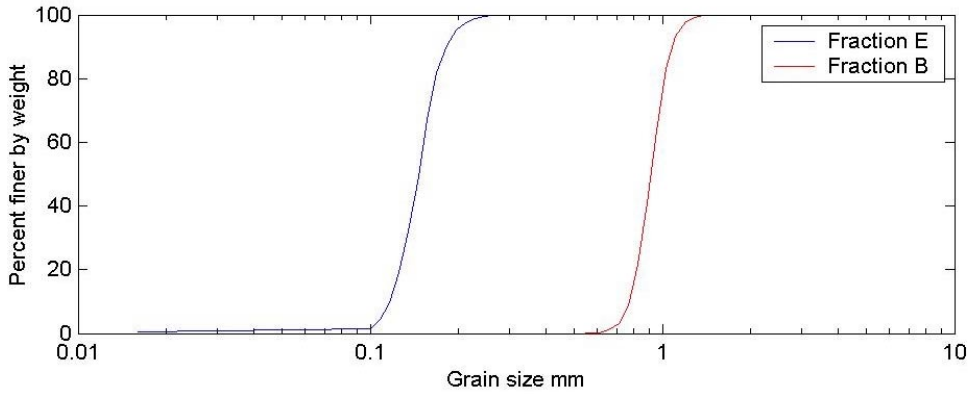

Figure 1: Particle size distributions for fraction E and fraction B silica sands.

Once sand has been poured to the final level, a lid is bolted to the top of the ESB box, with pump grease being applied to the joint to achieve a seal. A vacuum of greater than 95 kPa is then applied to the box to remove trapped air from the pore spaces. This ensures even saturation of the model as the silicone oil does not need to displace air from the pores and also increases the speed of seepage due to the enhanced pressure gradient between the oil reservoir and the model container. This does however introduce problems of sand boiling if oil is admitted at too great a speed. Silicone oil is then admitted to the base of the model through feed pipes fitted with needle valves to control flow-rate. A flow rate of 0.5 $kghr^{-1}$ per feed pipe was found to be sufficiently low to prevent piping of the model whilst still allowing saturation to be achieved in approximately 10 hours. The feed pipes are located in the reservoirs at top and bottom of the slope and consist of 8 mm diameter pipe with holes drilled at intervals to spread the oil across the model.

2.2 Test Procedure

After model preparation was complete, the SAM actuator and counterweight were loaded onto the centrifuge arm. The SAM was placed on a wooden block to make it hang level. The ESB box and shaking table were then ballasted with weights to make them hang horizontally from the crane and were lowered into place on the SAM. The SAM and ESB box were loaded separately onto the centrifuge in order to minimise model disturbance, as the oil-saturated slope is fairly unstable at 1 g.

Once the ESB box was in place on the SAM, wires from the instruments present in the model were connected to the junction boxes on the SAM and cable-tied into place.

After pre-flight checks had taken place, including such items as checking that enough pressure was available in the accumulator to fire earthquakes, the centrifuge was started and accelerated to 8g at which point both swinging platforms should have sat back against the end of the centrifuge arm. This was monitored by pairs of micro-switches at either end of the arm which are closed by the swing sitting against the end of the beam. The centrifuge speed at which this should occur for each swing

was calculated in the balance calculations and was compared with observed values as a safety check. In general (with SAM packages) the blue-end swing (SAM and ESB) swings up at 30 rpm and the red-end swing (counterweight) at 40 rpm.

Once both swings have swung up, the centrifuge was accelerated in stages to the required speed, in the case of the work described here 106 rpm or 50 g. Pore pressures were monitored during this acceleration stage in order to check the integrity of the package. When 50 g was reached, pumping commenced, with oil being admitted to the reservoir at the top of the slope and the sump being kept empty. Pore pressures within the model were monitored and oil was continuously admitted until a steady-state seepage regime was achieved with the water-table close to the surface of the slope.

When this condition was achieved, the model was ready to be subjected to an earthquake. Three-phase power was turned on to the SAM actuator and an offset was driven, changing the lever-arm length joining the package to the SAM. This was monitored by an LVDT (linearly variable displacement transducer) allowing a predictable earthquake magnitude to be achieved. Once this had been carried out, the compressed air supply to the clutch centring mechanism was turned on, forcing the clutch into a central position. The timer controlling the solid-state relays on the SAM package was then started, giving a ten second delay and then firing the earthquake. The timer also starts the data-acquisition system, which collects data during the earthquake and for a period afterwards.

After data-acquisition was complete, the data was uploaded from the CDAQS box and the decision was taken as to whether or not to fire subsequent earthquakes. If no further earthquakes were to be fired, the centrifuge was slowed and stopped. The SAM was then blocked up to hang level and the model was examined, measured and photographed.

3. Instrumentation

The models tested were instrumented with Birchall A23 accelerometers (ACC's) and Druck PDCR81 pore pressure transducers (PPT's) arranged throughout the sand of the model. The flexible piles used in tests SKH-13, 14 & 17 were also instrumented with strain gauges to measure bending moments and the piles in tests SKH-15-17 had Entran stress cells attached to them to measure contact stresses. Schematic instrumentation layouts for the centrifuge tests together with the coordinates of the instruments are shown in Figures 3 to 8 and Tables 3 to 7 respectively. The coordinate system used is x being the downslope coordinate from an origin at the end of the box, z being a vertical coordinate from the base of the ESB box and y the transverse coordinate from the edge of the box.

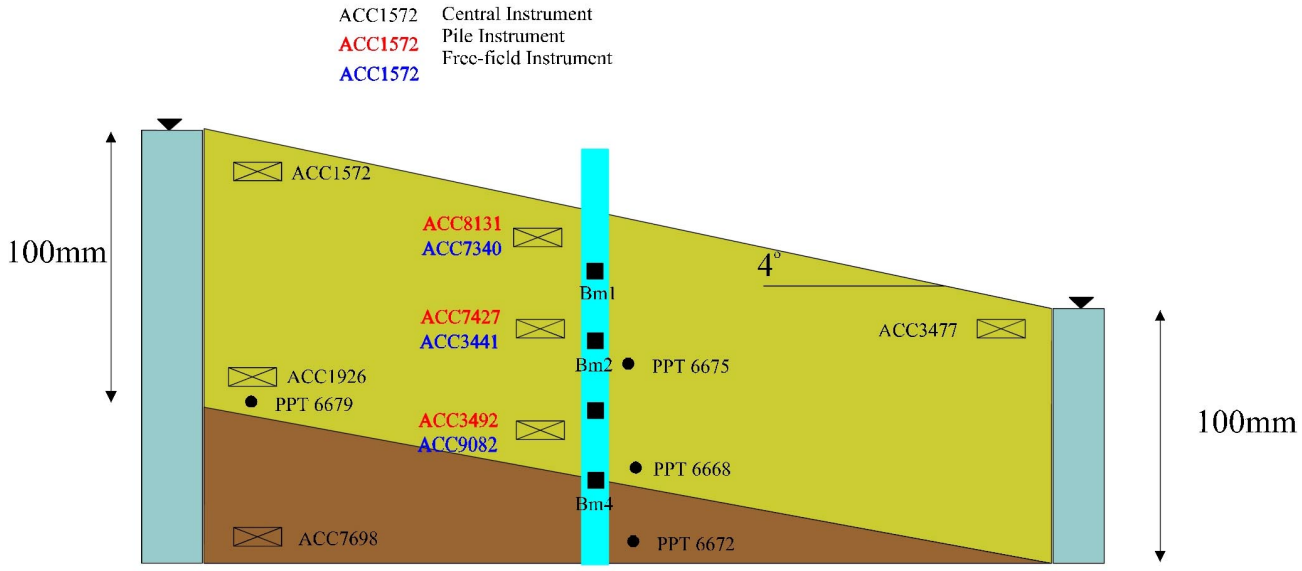

Figure 2: Instrument layout for test SKH-13

Table 3: Instrumentation coordinates for test SKH-13

Instrument	x (mm)	y (mm)	z (mm)
ACC1572	110	60	100
ACC1926	110	65	40
ACC3441	270	75	60
ACC3477	480	80	80
ACC3492	280	195	25
ACC7340	250	75	80
ACC7427	270	195	60
ACC7698	125	130	5
ACC8131	260	190	90
ACC8925	ESB bottom ring		
ACC9082	280	75	25
PPT6668	360	130	10
PPT6672	256	122	5
PPT6675	380	190	50
PPT6679	200	130	20

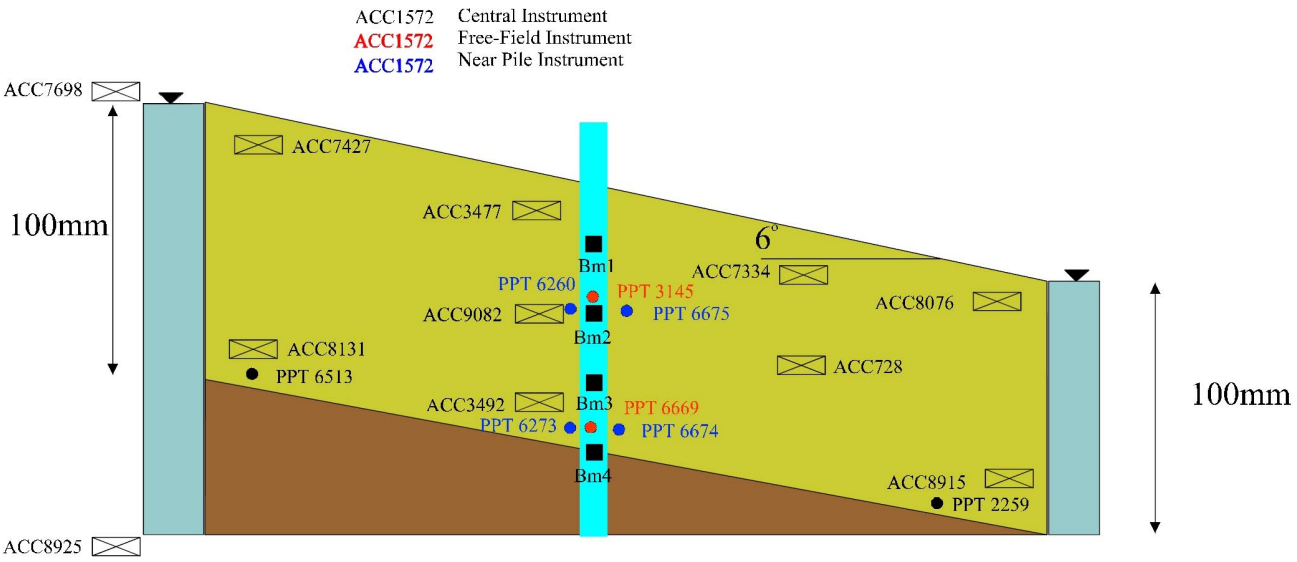

Figure 3: Instrument layout for test SKH-14

Table 4: Instrumentation coordinates for test SKH-14

Instrument	x (mm)	y (mm)	z (mm)
ACC3477	220	120	100
ACC3492	285	135	25
ACC728	365	120	60
ACC7334	330	120	90
ACC7427	120	120	110
ACC7698	ESB 4th ring		
ACC8076	450	120	75
ACC8131	120	160	60
ACC8915	390	115	10
ACC8925	ESB bottom ring		
ACC9082	230	125	75
PPT2259	470	125	10
PPT3145	230	120	70
PPT6260	260	60	70
PPT6273	260	60	30
PPT6513	140	110	40
PPT6669	270	120	30
PPT6674	305	60	25
PPT6675	300	60	70

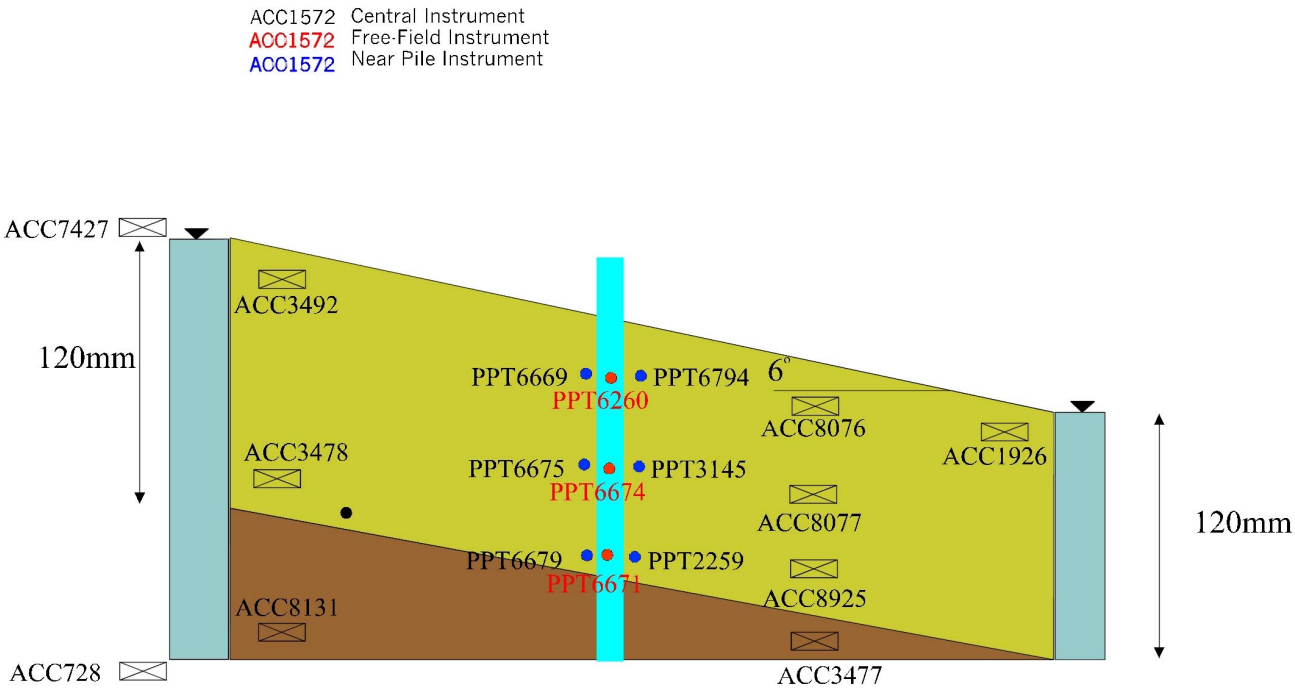

Figure 4: Instrument layout for test SKH-15

Table 5: Instrumentation coordinates for test SKH-15

Instrument	x (mm)	y (mm)	z (mm)
ACC1926	440	120	110
ACC3477	387	97	5
ACC3478	120	95	50
ACC3492	115	115	140
ACC728	ESB bottom ring		
ACC7427	ESB 4th ring		
ACC8076	365	120	110
ACC8077	370	125	80
ACC8131	135	100	15
ACC8925	370	95	25
PPT2259	310	60	65
PPT3145	310	60	90
PPT6260	260	130	110
PPT6273	165	160	50
PPT6669	260	60	110
PPT6671	300	115	60
PPT6674	240	115	90
PPT6675	260	60	90
PPT6679	263	60	65
PPT6794	310	60	110

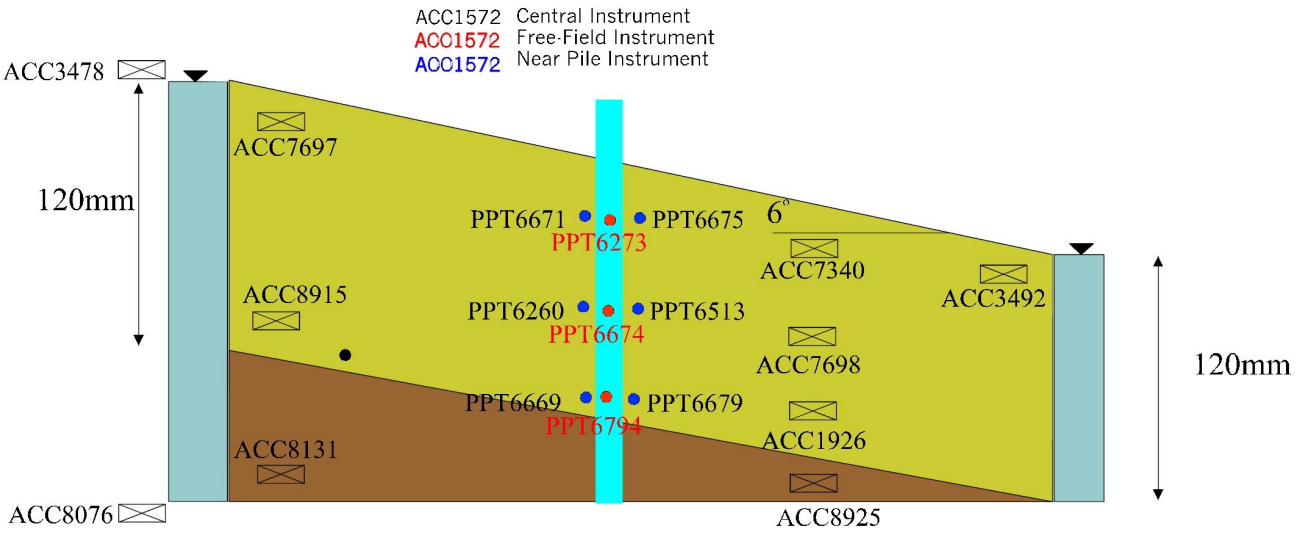

Figure 5: Instrument layout for test SKH-16

Table 6: Instrumentation coordinates for test SKH-16

Instrument	x (mm)	y (mm)	z (mm)
ACC1926	365	90	20
ACC3478	ESB 4th ring		
ACC7698	375	140	80
ACC8076	ESB bottom ring		
ACC8131	140	130	5
ACC8915	90	95	40
ACC8925	410	145	5
PPT2259	180	95	40
PPT6260	260	55	85
PPT6273	240	115	115
PPT6513	310	55	80
PPT6669	260	55	60
PPT6671	260	55	120
PPT6674	250	120	80
PPT6675	315	55	120
PPT6679	310	55	55
PPT6794	275	115	60

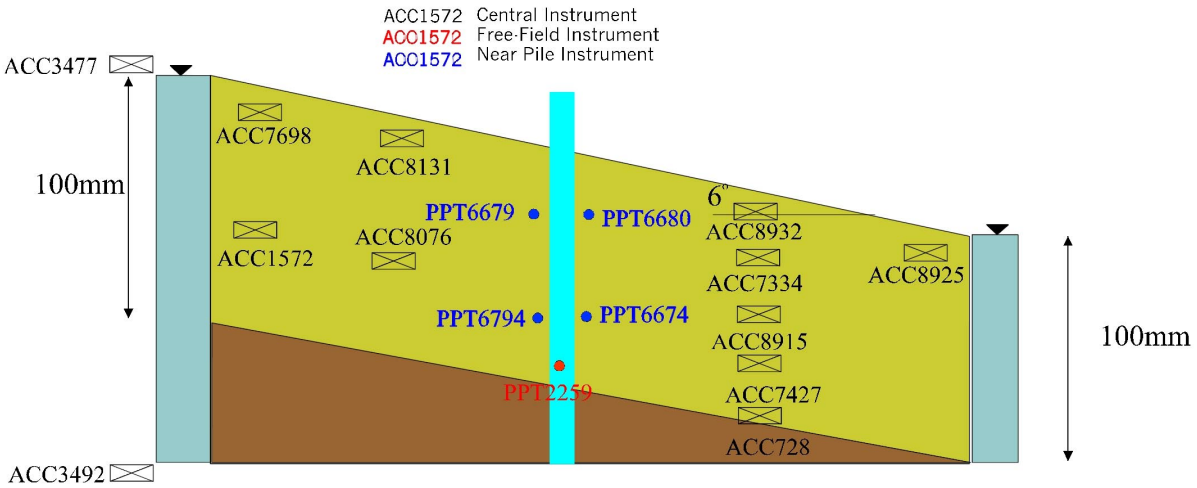

Figure 6: Instrument layout for test SKH-17

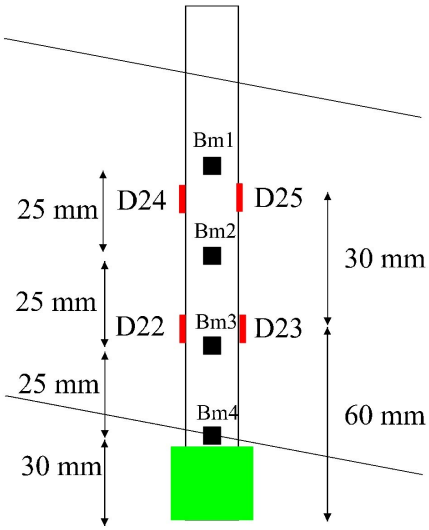

Figure 7: Pile instrumentation in test SKH-17

Table 7: Instrumentation coordinates for test SKH-17

Instrument	x (mm)	y (mm)	z (mm)
ACC1572	95	130	60
ACC3477	ESB 4th ring		
ACC3492	ESB bottom ring		
ACC6794	250	60	60
ACC728	395	140	10
ACC7334	360	160	75
ACC7427	390	130	30
ACC7698	140	105	130
ACC8076	225	120	60
ACC8131	230	110	120
ACC8915	360	120	50
ACC8925	470	110	80
ACC8932	380	100	100
PPT2259	228	115	25
PPT6674	300	60	60
PPT6679	260	60	90
PPT6680	300	60	90

4. Results

Time-histories of acceleration and pore-pressure for the centrifuge tests are shown in Figures 9 through 24. Only a brief discussion of the results will be made here, further discussion can be found in Haigh (2002).

4.1 Test SKH-13

The results of this test are plotted in Figures 9-11. This test consisted of a single circular flexible pile in a liquefiable slope. I can be seen that significant attenuation of acceleration is observed at the surface of the model due to liquefaction and that a base bending moment of 1.5 Nm is induced in the pile. It can also be seen that significant dilation occurs at PPT6675, close to the pile at the centre of the liquefiable layer.

4.2 Test SKH-14

The results for test SKH-14 are plotted in Figures 12-14. In this test, two flexible piles of circular and square section were tested. Instrumentation to measure pore-pressures close to the front and back faces of the pile was used to pick up near-field behaviour. Again significant attenuation of acceleration is noted close to the model surface. Very high dilation is noted close to the pile, particularly downslope of the pile, where dilation to almost zero gauge pressure is noted. This would cause large hydrodynamic forces to be experienced by the piles. The bending moments shown in Figure 14 show unexpected trends owing to plastic failure of the piles.

4.3 Test SKH-15

The results of this test are plotted in Figures 15-17. This test contained circular and square section rigid brass piles, instrumented with Entran pressure transducers to measure contact stresses. PPT's close to the pile again show significant dilative behaviour., which was also picked up by the stress cells. Comparison of pressures on the upslope and downslope faces of the piles shows a large net downslope force being exerted on the piles by the flowing soil.

4.4 Test SKH-16

The results of test SKH-16 are plotted in Figures 18-20. This test was identical to test SKH-15 but the circular pile was instrumented with stress cells, rather than the square one. Similar results were achieved as in test SKH-15, with slightly noisy data being gained owing to a new data-acquisition setup being tested which was seen to be prone to interference from the SAM actuator motor.

4.5 Test SKH-17

The results of test SKH-17 are plotted in Figures 21-24. This test contained flexible piles of circular and square cross-sections, instrumented to measure both contact stresses and bending moments. It

was seen that similar stresses to those measured in tests SKH-15 & 16 were measured on the piles, though the magnitude of the cycling of the stresses was reduced owing to pile flexibility. Comparison of the results of measuring applied stresses and induced bending moments showed that the bending moments measured during the earthquake were substantially lower than those which would be predicted by assuming equilibrium of the pile, though this was not true of residual post-earthquake values. This can be explained as the pile need not be in equilibrium at all times during a dynamic event.

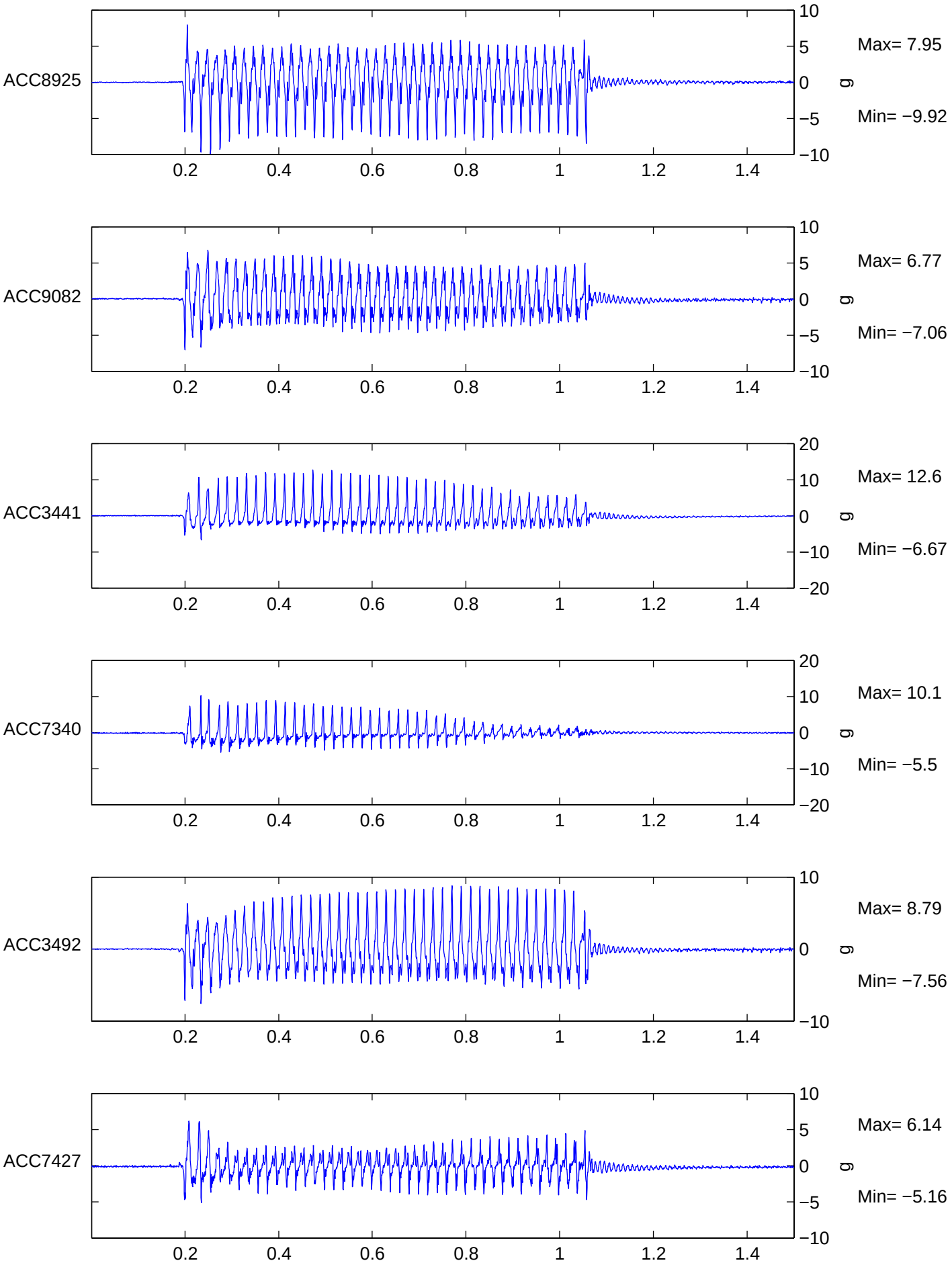

TEST SKH−13 FLIGHT 1		Scales: Model 8th order Butterworth Filter at 500Hz Short−Term Time Records	Earthquake 1	Figure No. 9a

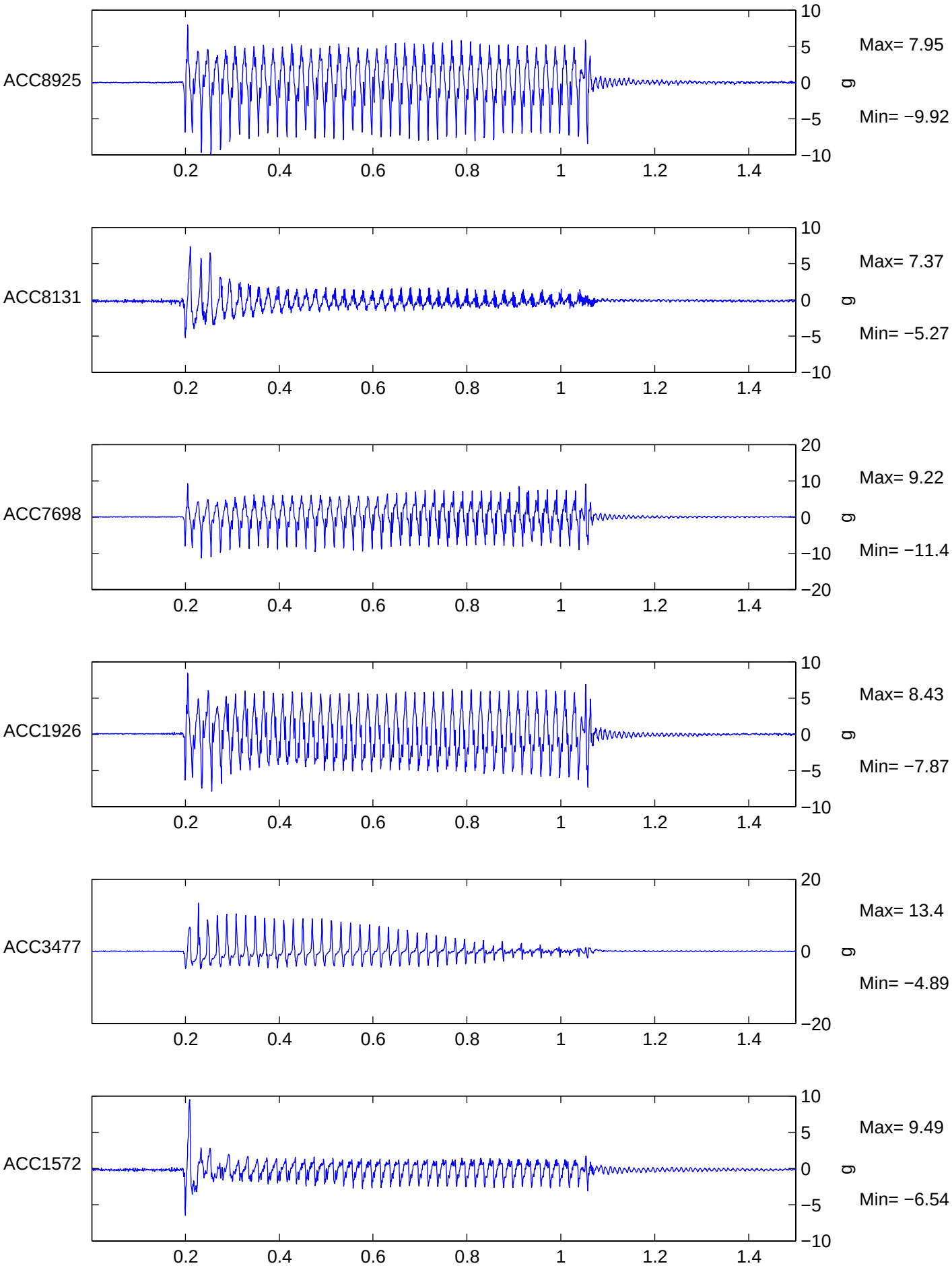

TEST SKH−13 FLIGHT 1		Scales: Model 8th order Butterworth Filter at 500Hz Short−Term Time Records	Earthquake 1	Figure No. 9b

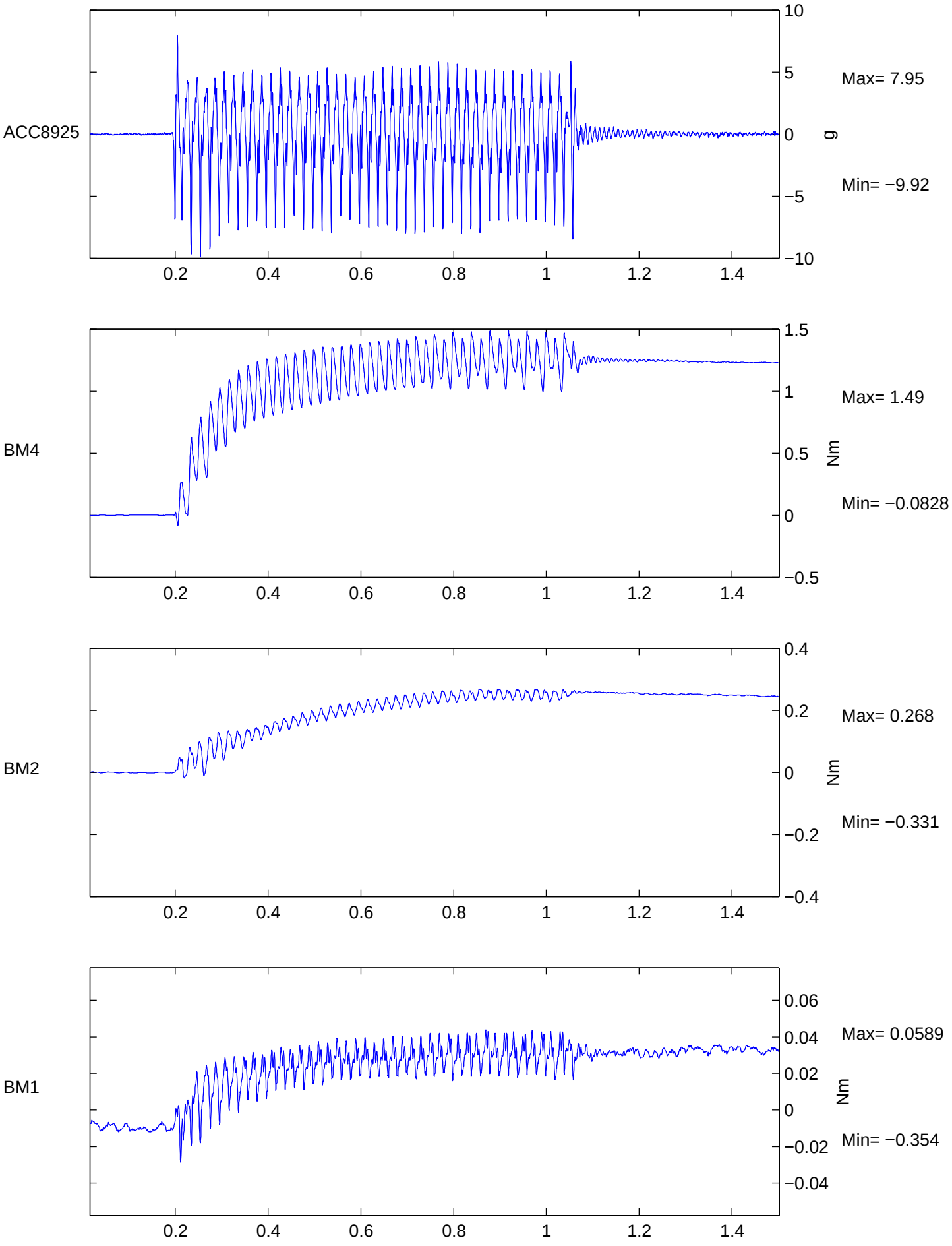

TEST SKH−13 FLIGHT 1		Scales: Model 8th order Butterworth Filter at 500Hz Short−Term Time Records	Earthquake 1	Figure No. 10

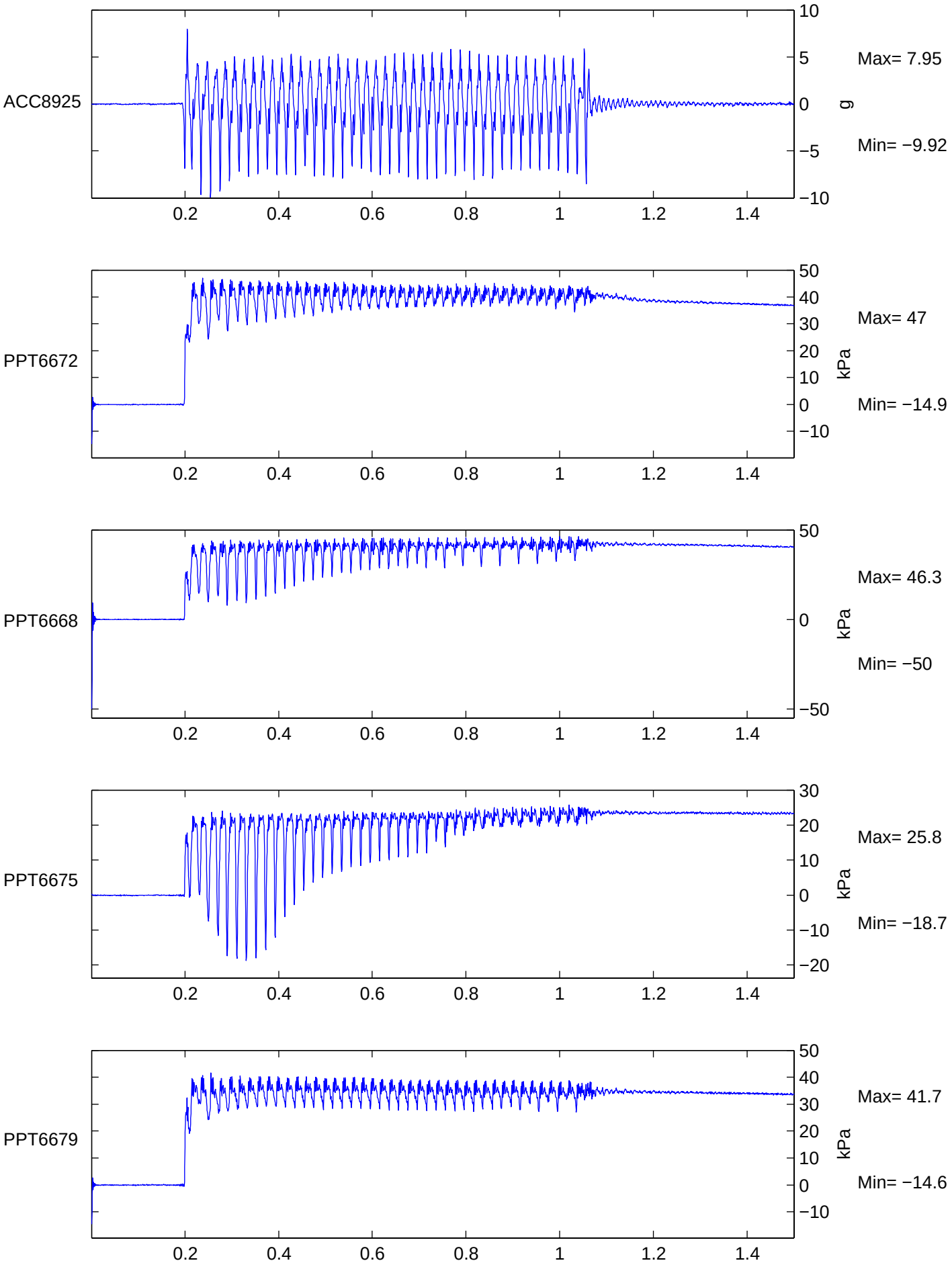

TEST SKH−13 FLIGHT 1		Scales: Model 8th order Butterworth Filter at 500Hz Short−Term Time Records	Earthquake 1	Figure No. 11

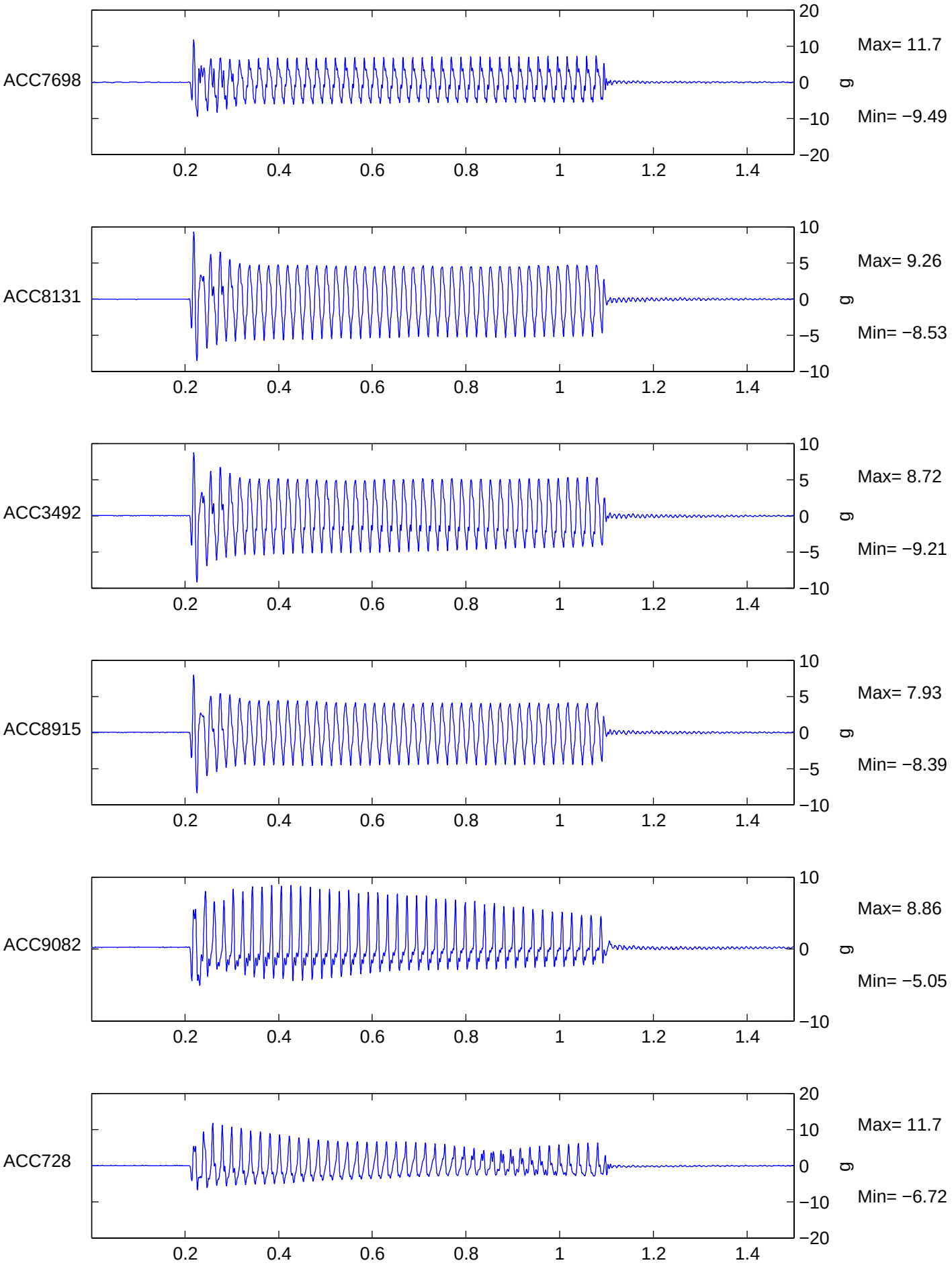

TEST SKH−14 FLIGHT 1		Scales: Model 8th order Butterworth Filter at 200Hz Short−Term Time Records	Earthquake 1	Figure No. 12a

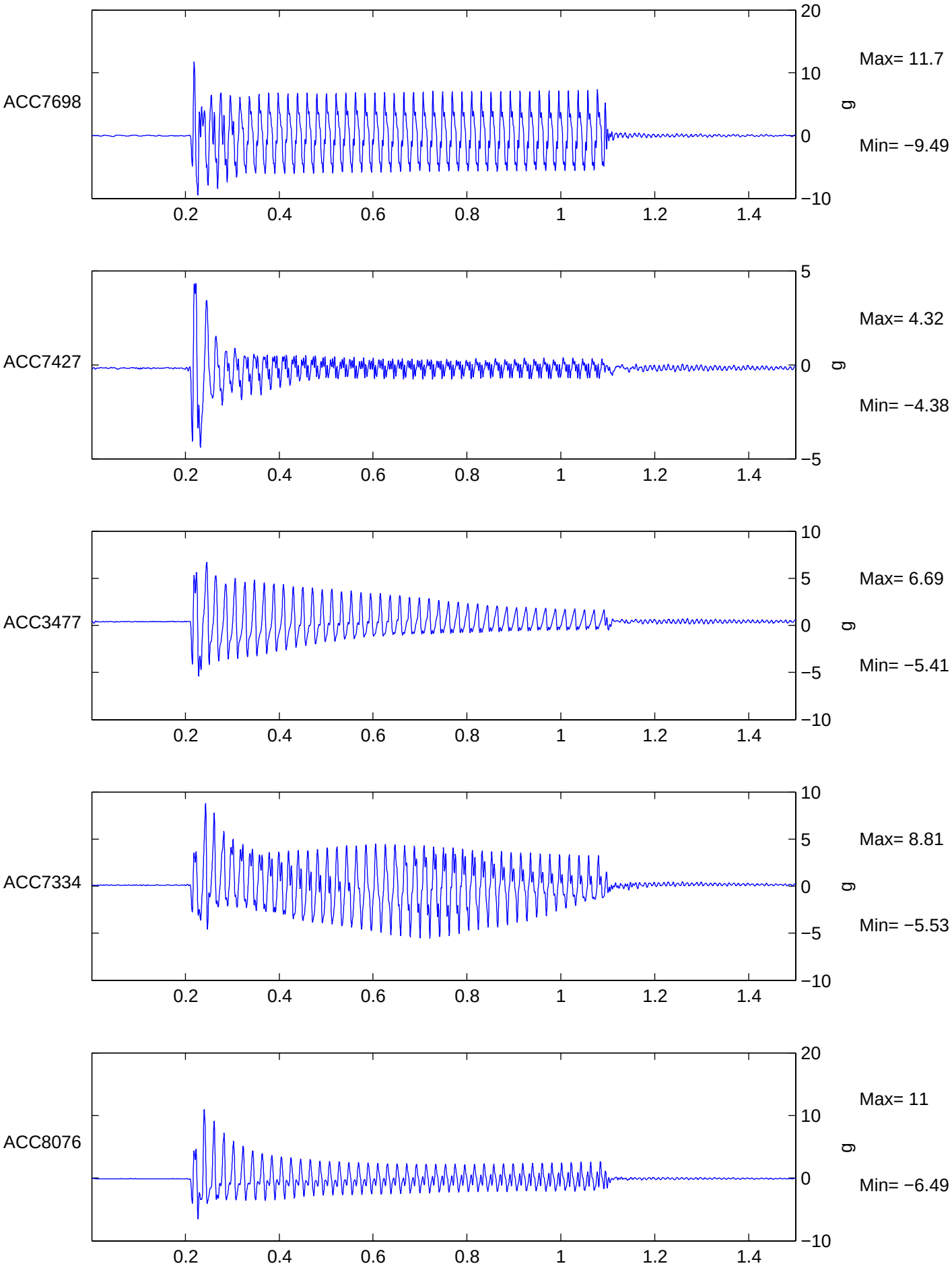

TEST SKH−14 FLIGHT 1		Scales: Model 8th order Butterworth Filter at 200Hz Short−Term Time Records	Earthquake 1	Figure No. 12b

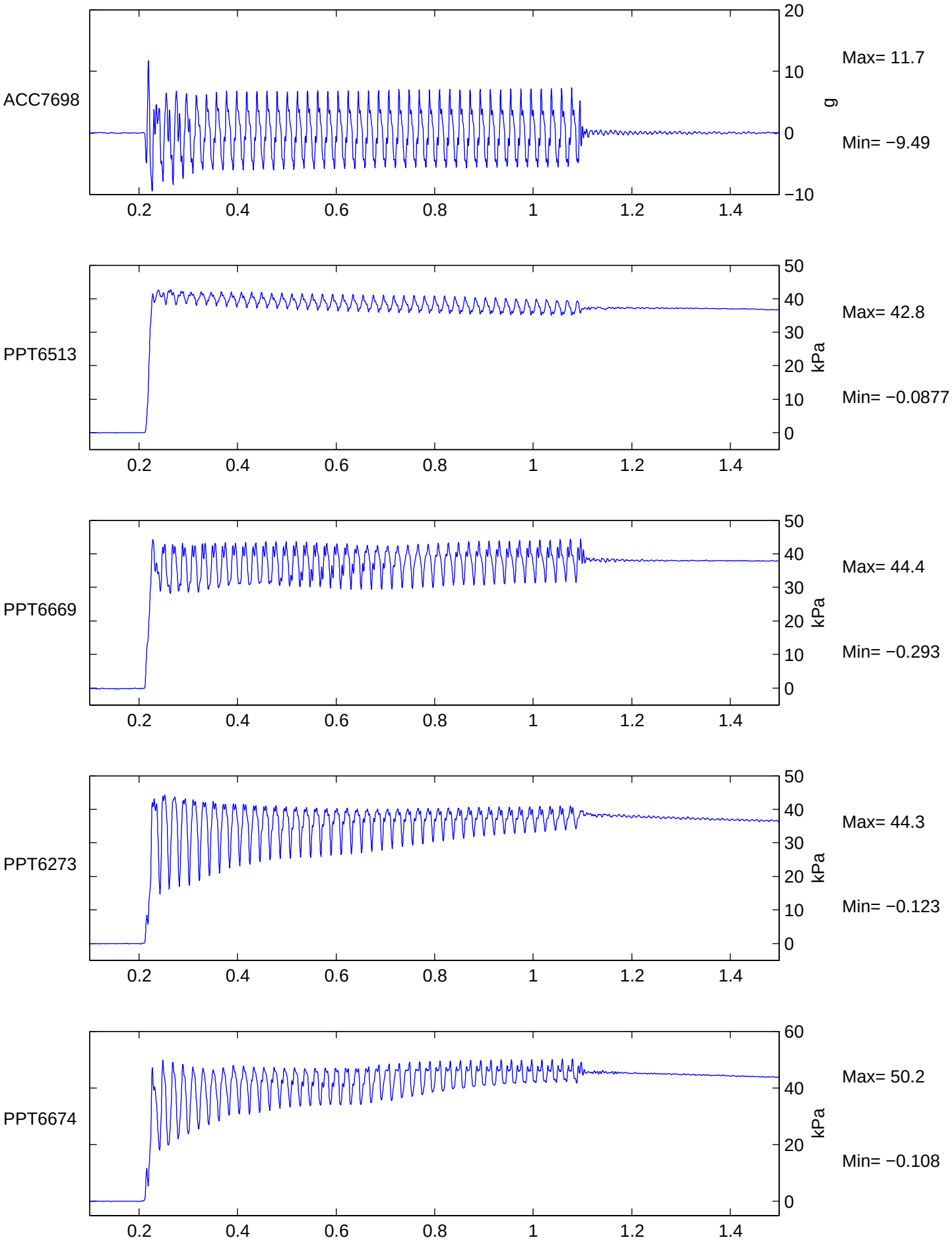

TEST SKH−14 FLIGHT 1		Scales: Model 8th order Butterworth Filter at 200Hz Short−Term Time Records	Earthquake 1	Figure No. 13a

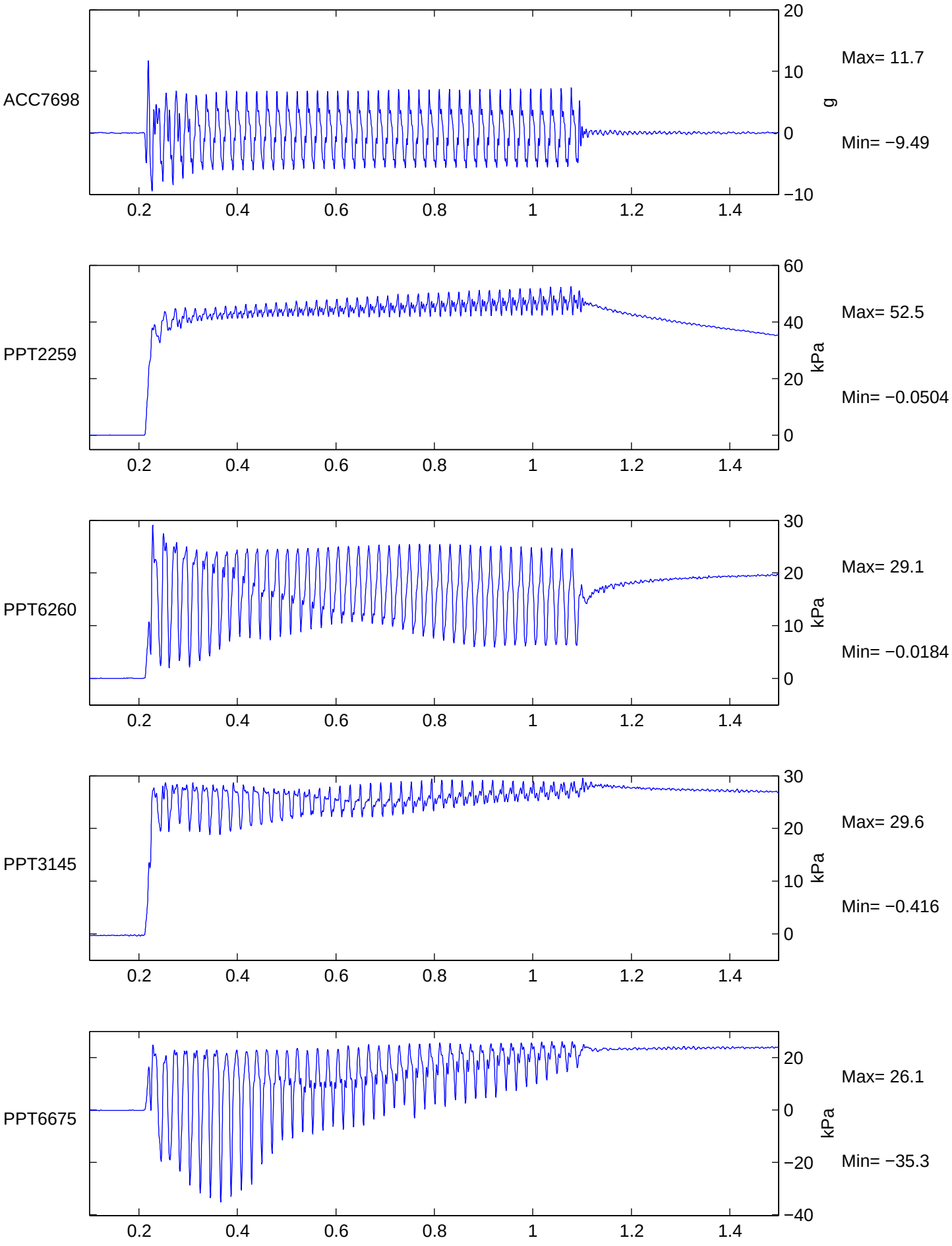

TEST SKH−14 FLIGHT 1		Scales: Model 8th order Butterworth Filter at 200Hz Short−Term Time Records	Earthquake 1	Figure No. 13b

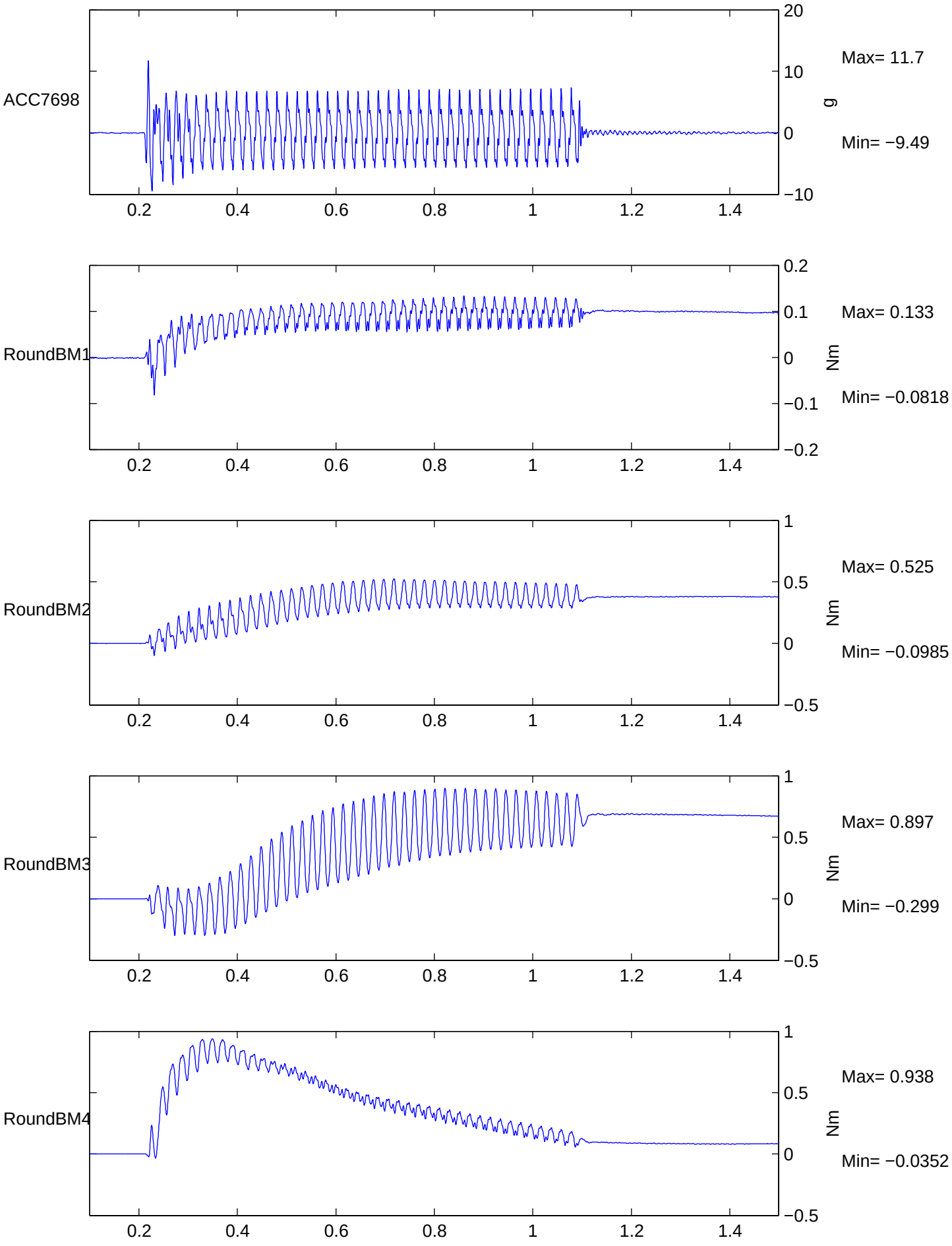

TEST SKH−14 FLIGHT 1		Scales: Model 8th order Butterworth Filter at 200Hz Short−Term Time Records	Earthquake 1	Figure No. 14a

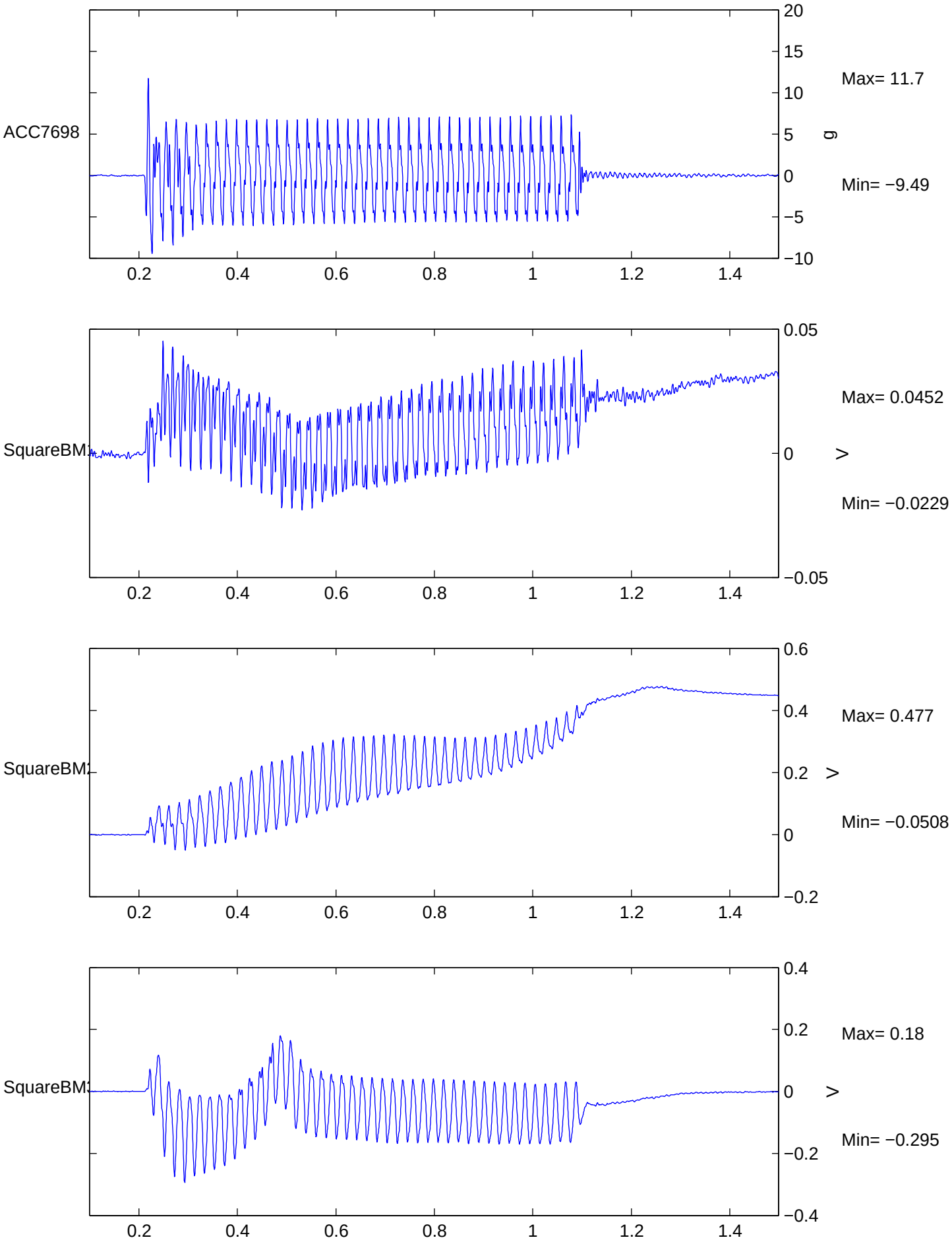

TEST SKH−14 FLIGHT 1		Scales: Model 8th order Butterworth Filter at 200Hz Short−Term Time Records	Earthquake 1	Figure No. 14b

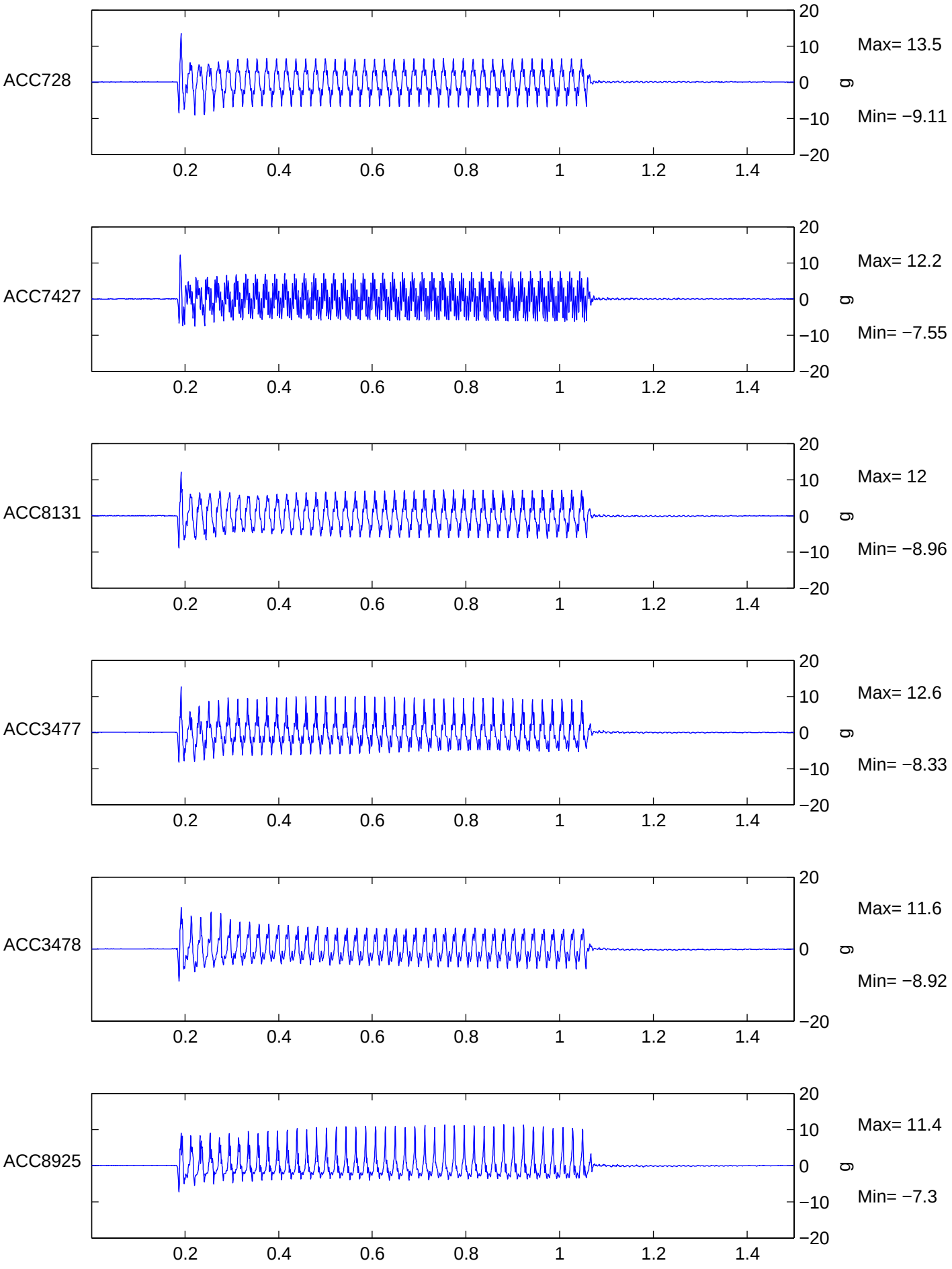

TEST SKH−15 FLIGHT 1		Scales: Model 8th order Butterworth Filter at 500Hz Short−Term Time Records	Earthquake 1	Figure No. 15a

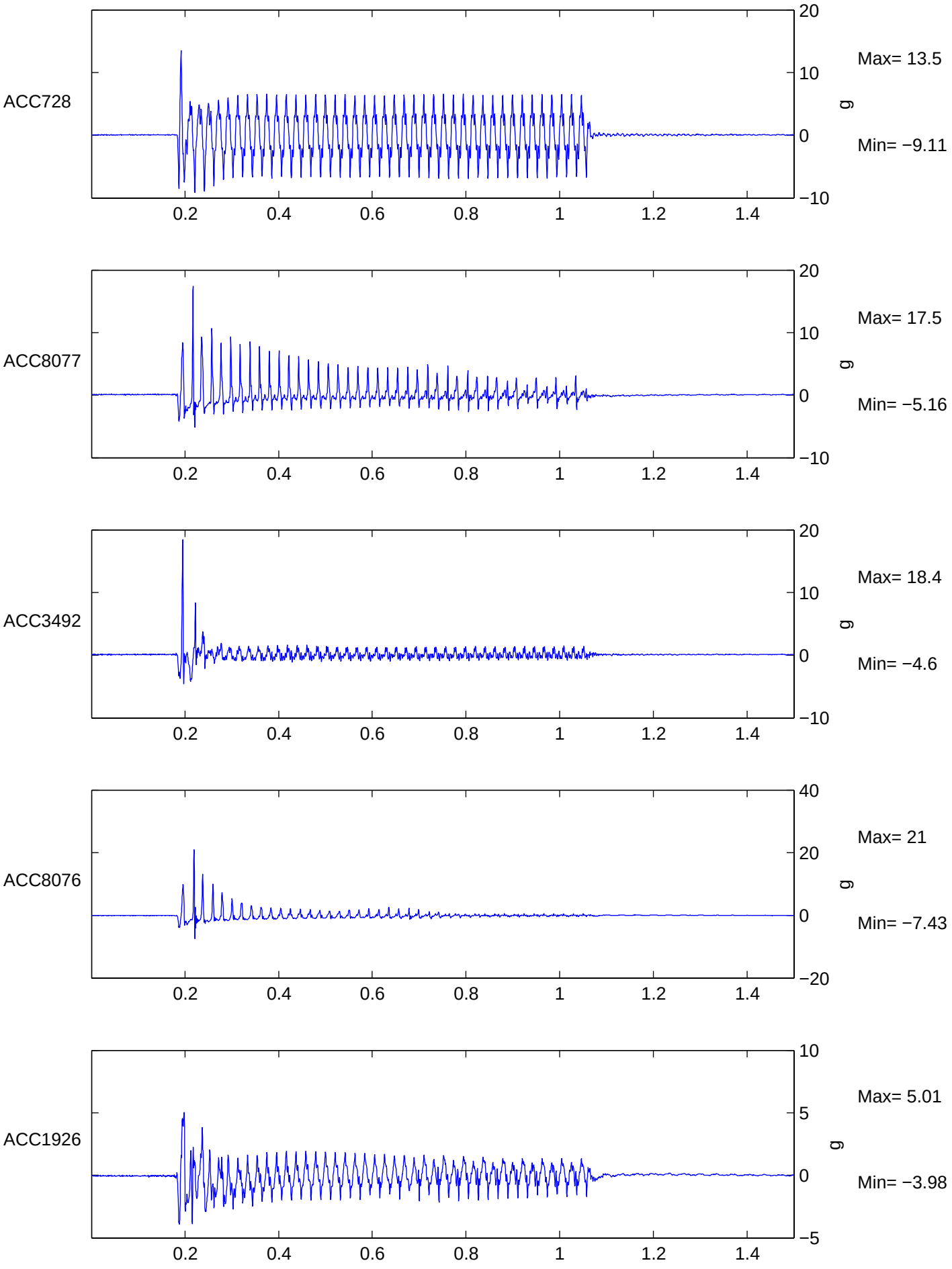

TEST SKH−15 FLIGHT 1		Scales: Model 8th order Butterworth Filter at 500Hz Short−Term Time Records	Earthquake 1	Figure No. 15b

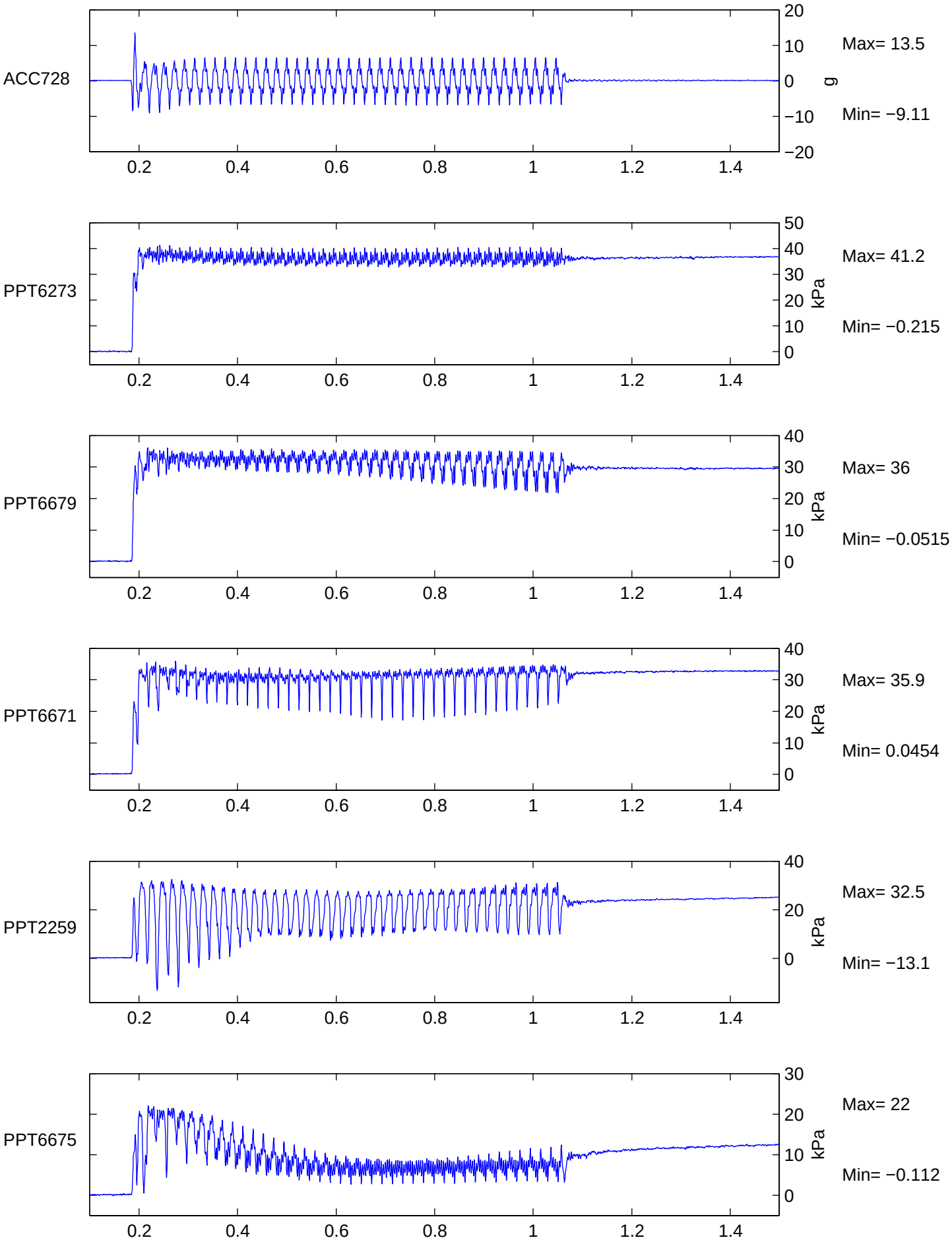

TEST SKH−15 FLIGHT 1		Scales: Model 8th order Butterworth Filter at 500Hz Short−Term Time Records	Earthquake 1	Figure No. 16a

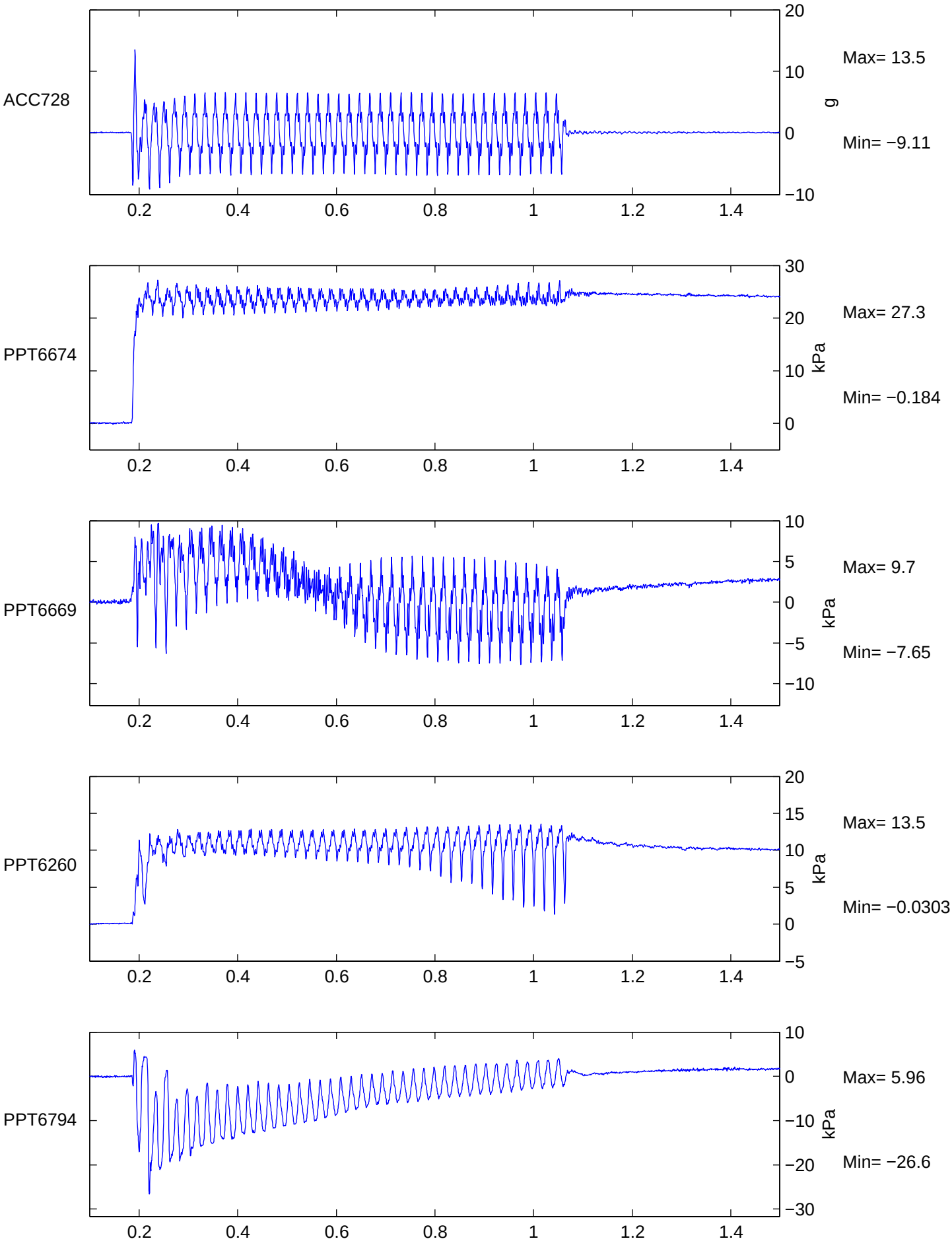

TEST SKH−15 FLIGHT 1		Scales: Model 8th order Butterworth Filter at 500Hz Short−Term Time Records	Earthquake 1	Figure No. 16b

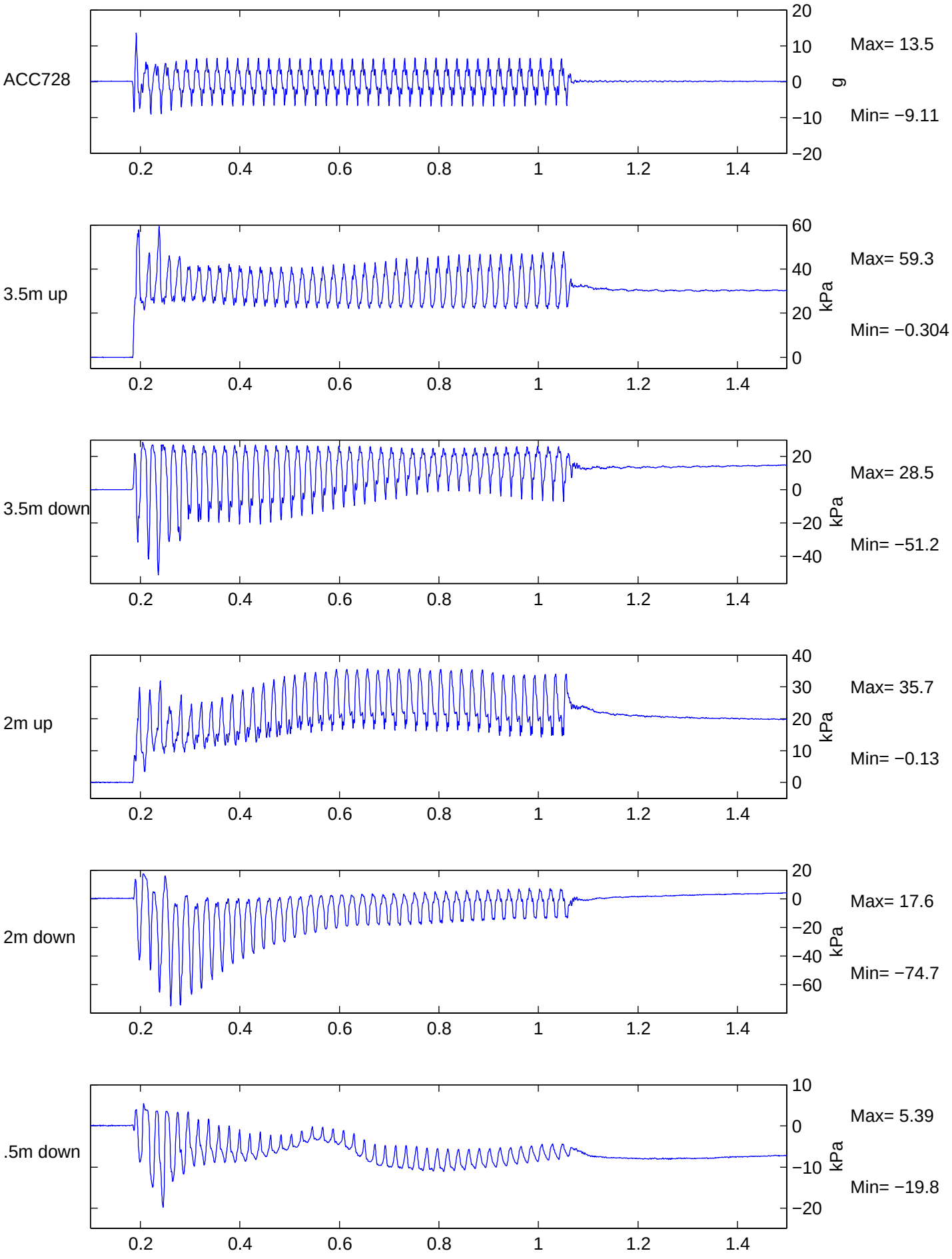

TEST SKH−15 FLIGHT 1		Scales: Model 8th order Butterworth Filter at 500Hz Short−Term Time Records	Earthquake 1	Figure No. 17

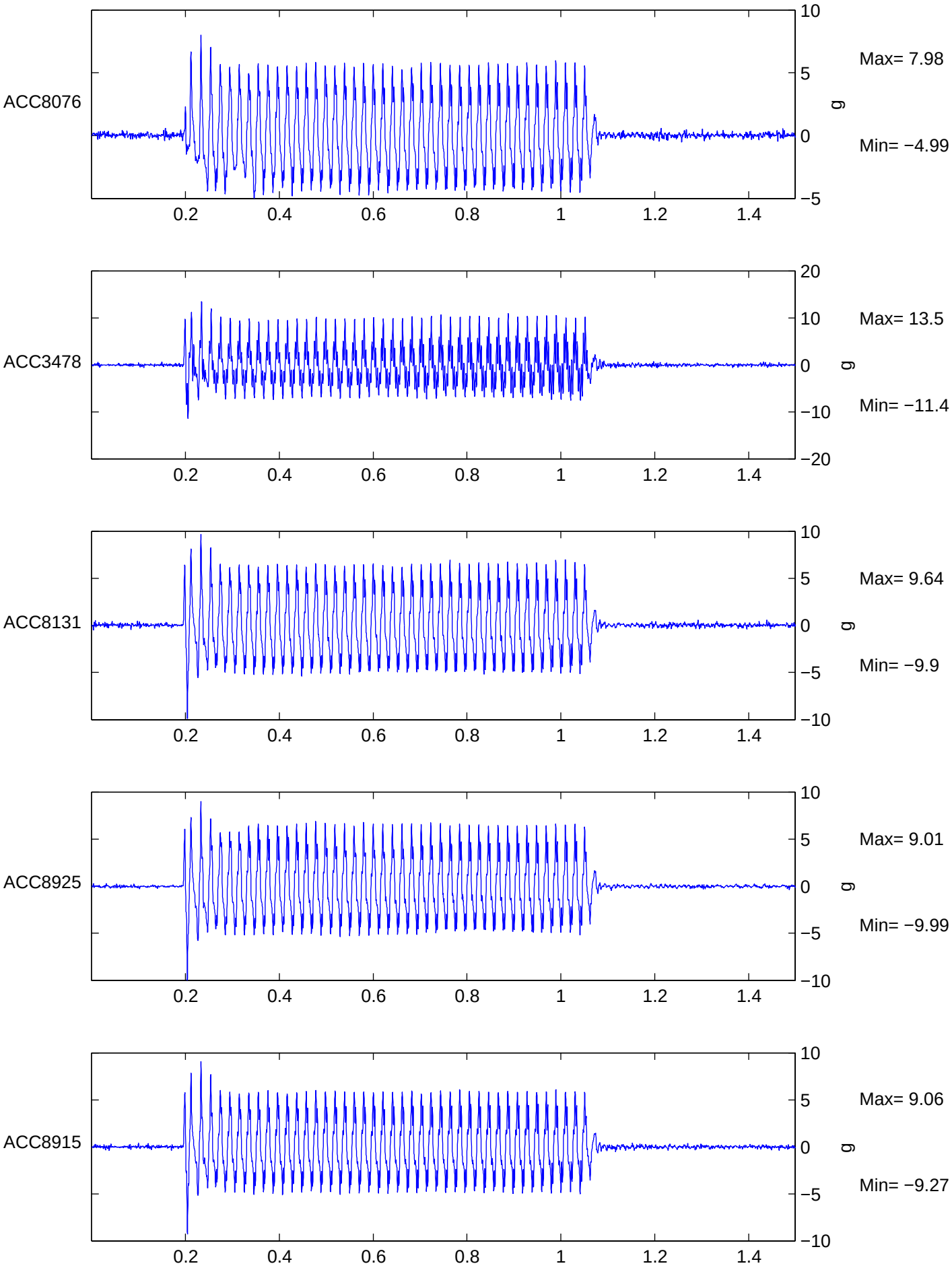

TEST SKH16 FLIGHT 1		Scales: Model 8th order Butterworth Filter at 500Hz Short−Term Time Records	Earthquake 1	Figure No. 18a

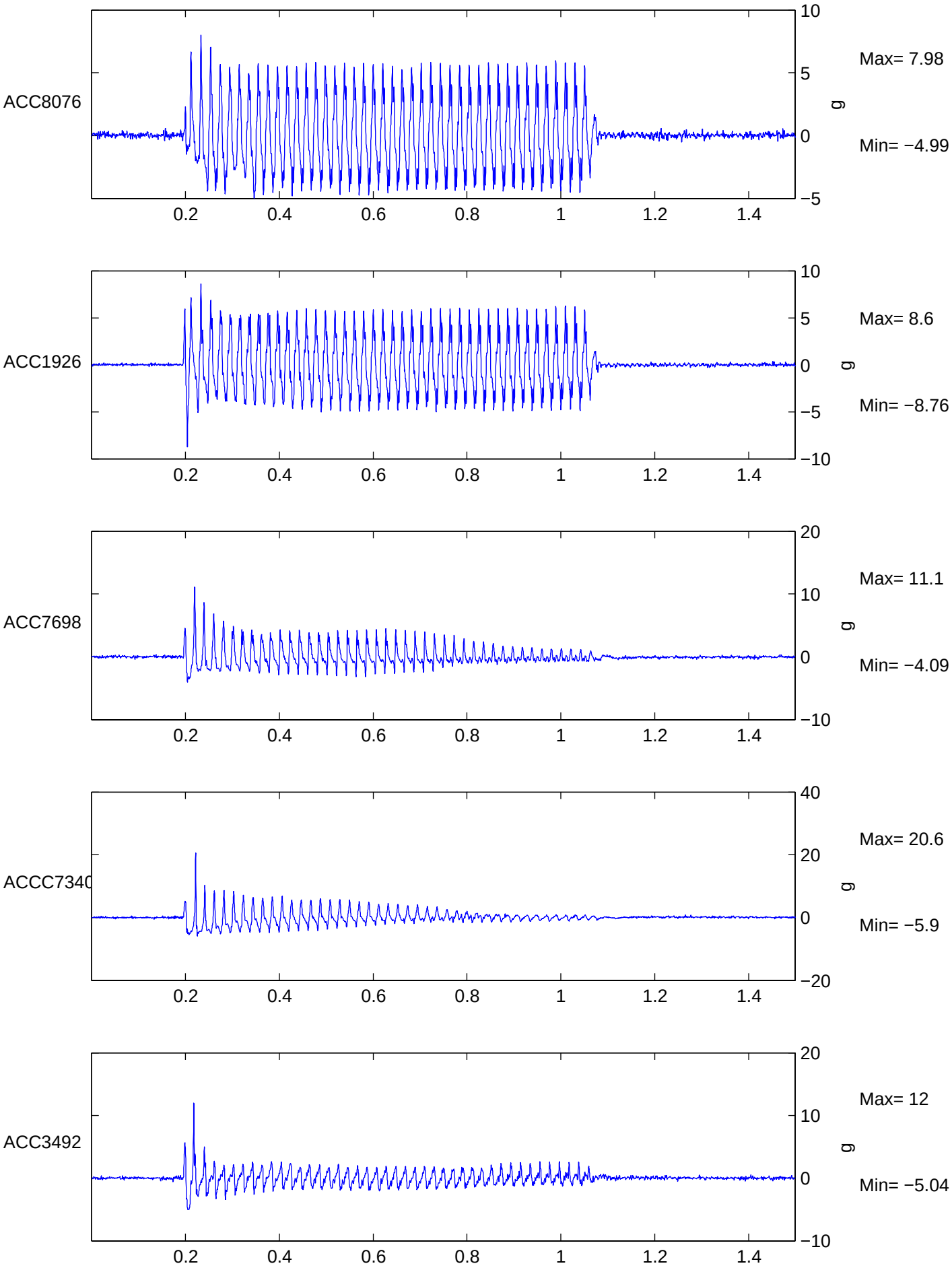

TEST SKH16 FLIGHT 1		Scales: Model 8th order Butterworth Filter at 500Hz Short−Term Time Records	Earthquake 1	Figure No. 18b

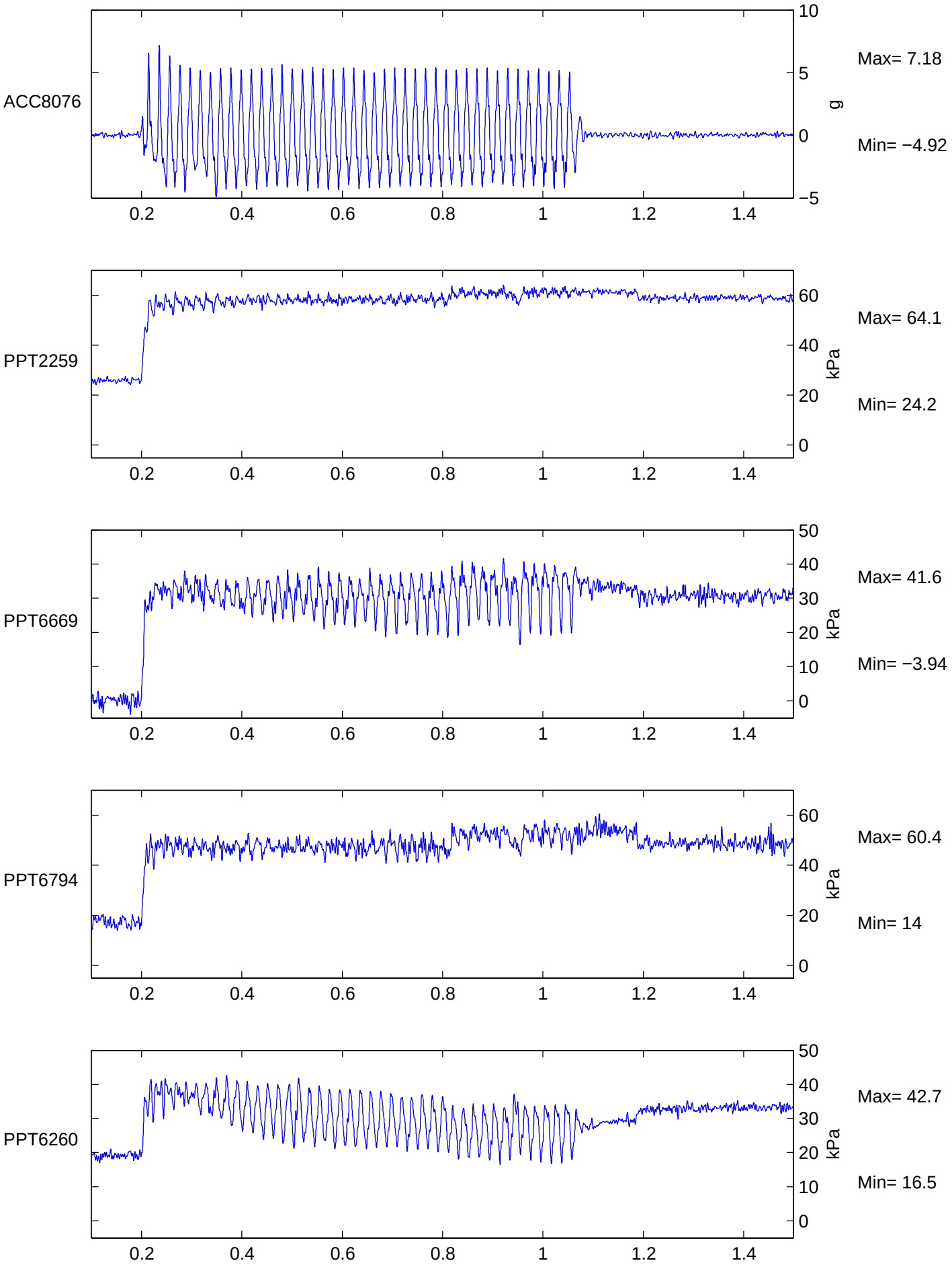

TEST SKH16 FLIGHT 1		Scales: Model 8th order Butterworth Filter at 250Hz Short−Term Time Records	Earthquake 1	Figure No. 19a

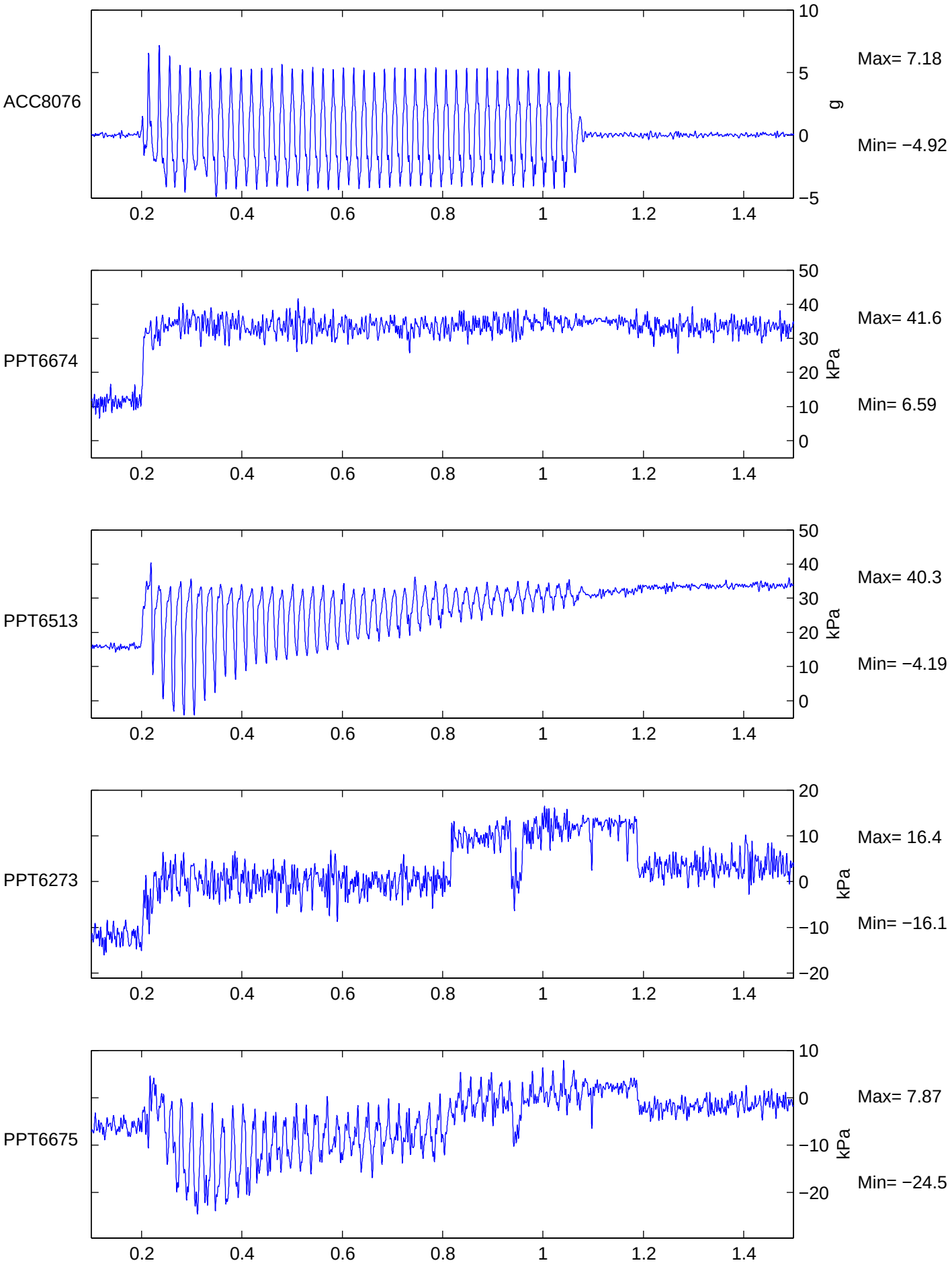

TEST SKH16 FLIGHT 1		Scales: Model 8th order Butterworth Filter at 250Hz Short−Term Time Records	Earthquake 1	Figure No. 19b

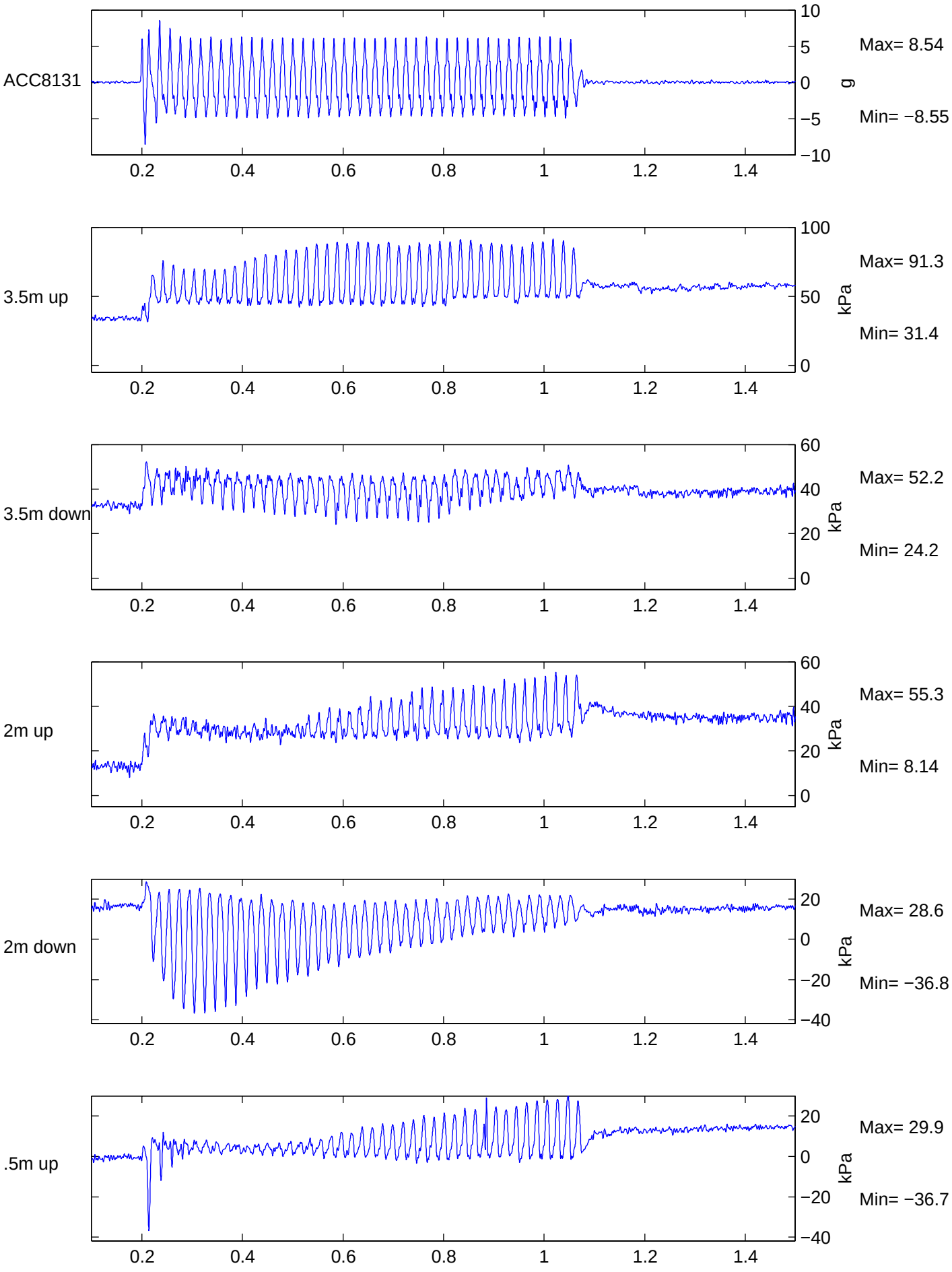

TEST SKH16 FLIGHT 1		Scales: Model 8th order Butterworth Filter at 250Hz Short−Term Time Records	Earthquake 1	Figure No. 20

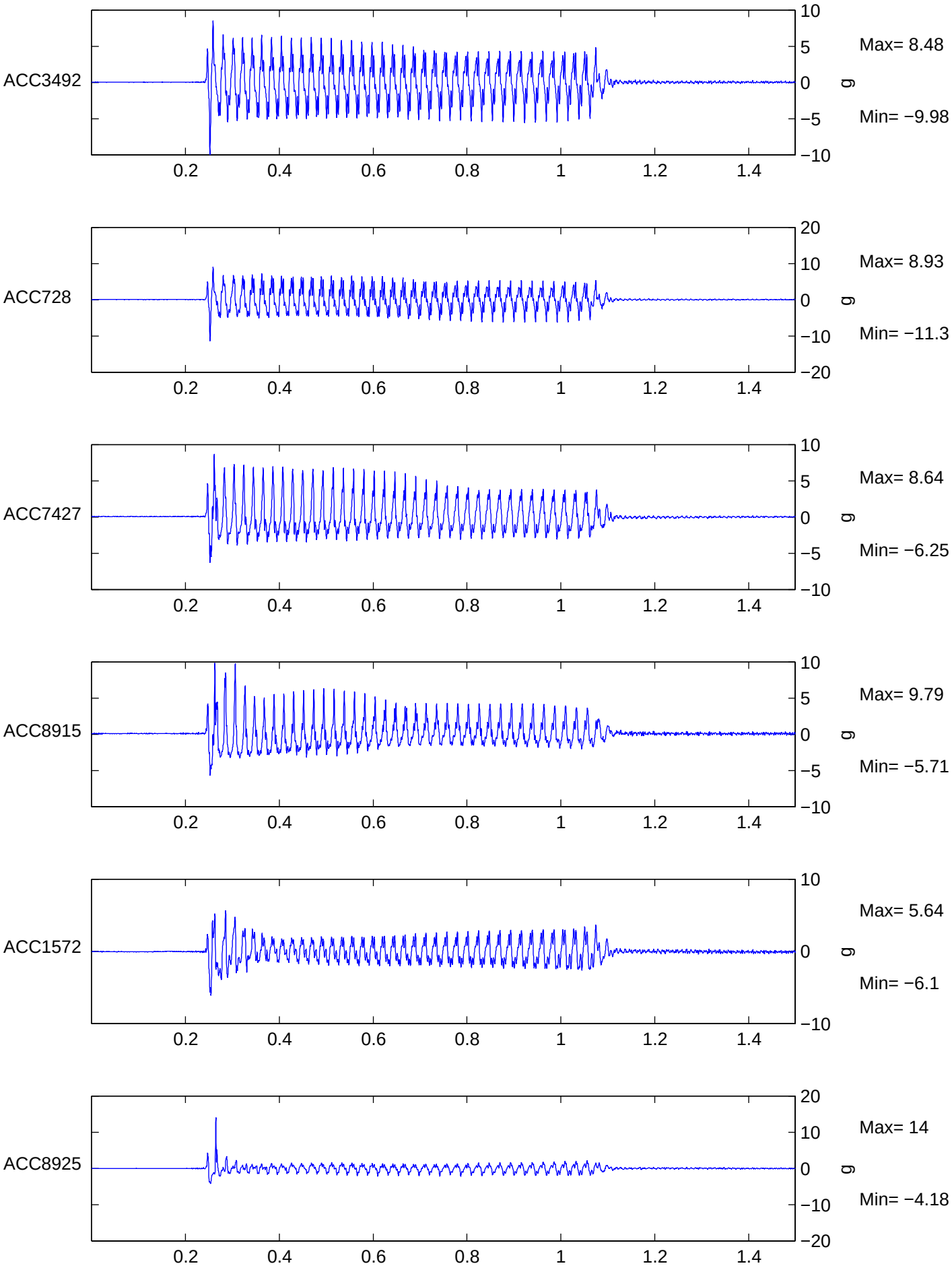

TEST SKH−17 FLIGHT 1		Scales: Model 8th order Butterworth Filter at 500Hz Short−Term Time Records	Earthquake 1	Figure No. 21a

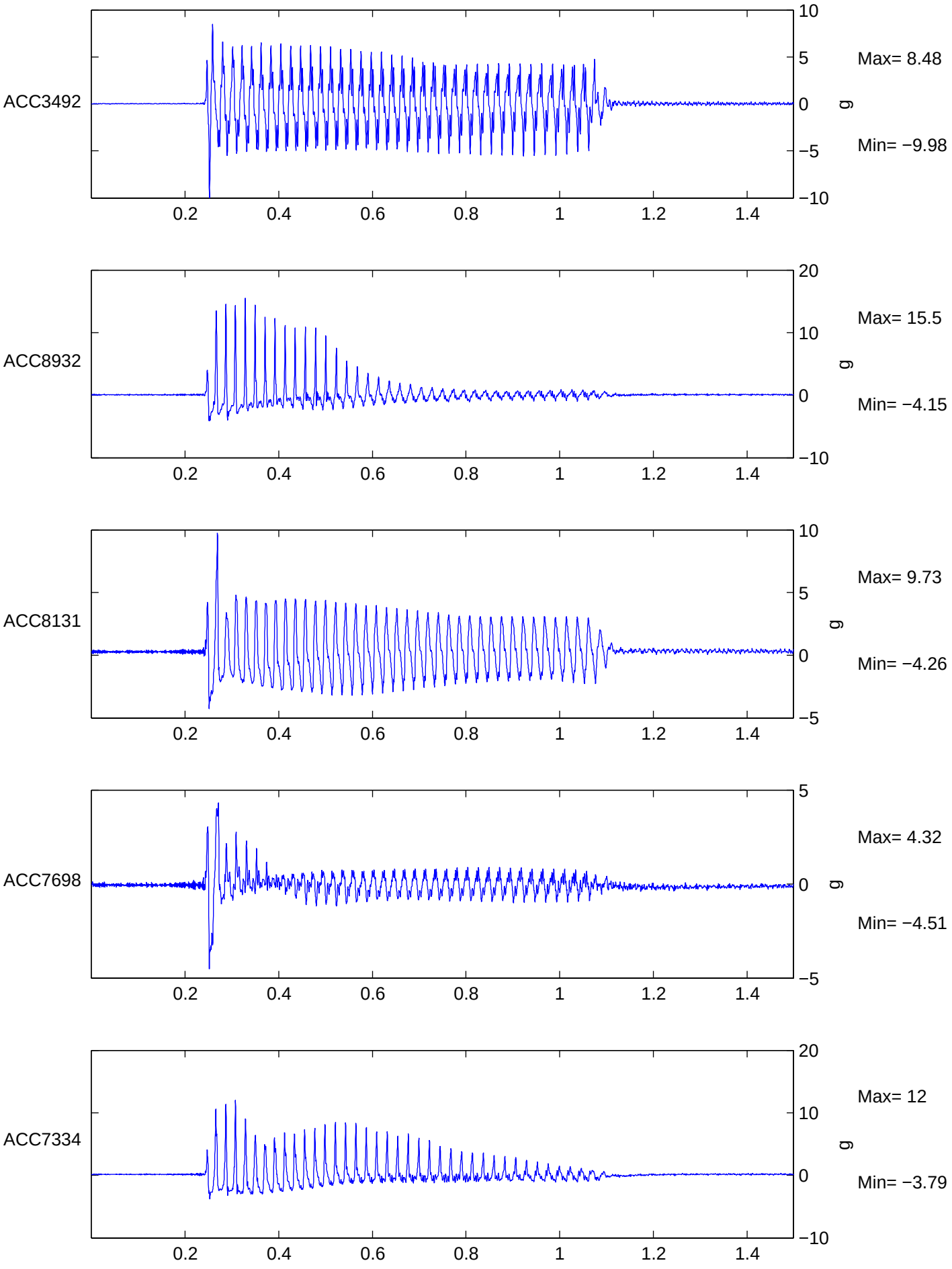

TEST SKH−17 FLIGHT 1		Scales: Model 8th order Butterworth Filter at 500Hz Short−Term Time Records	Earthquake 1	Figure No. 21b

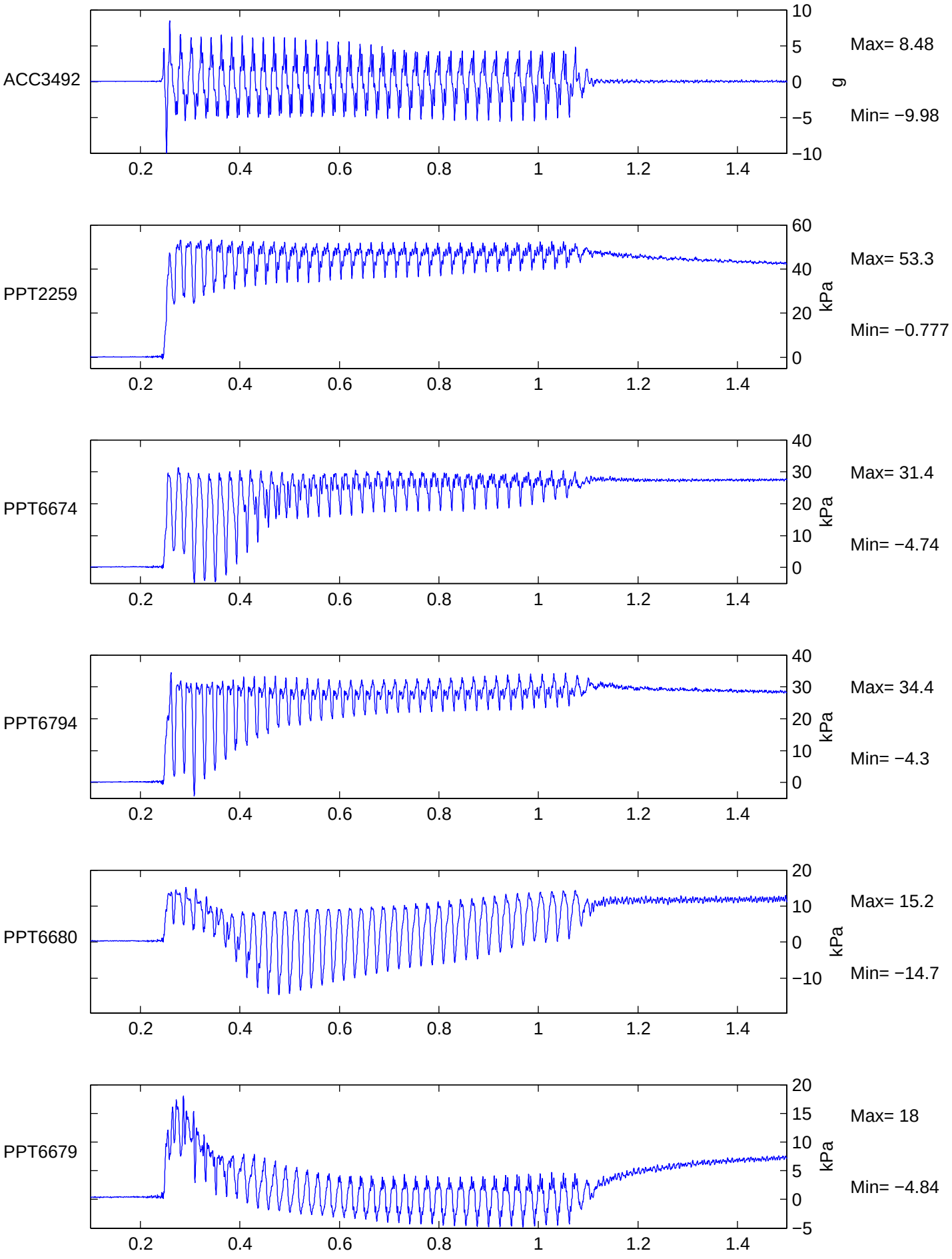

TEST SKH−17 FLIGHT 1		Scales: Model 8th order Butterworth Filter at 500Hz Short−Term Time Records	Earthquake 1	Figure No. 22

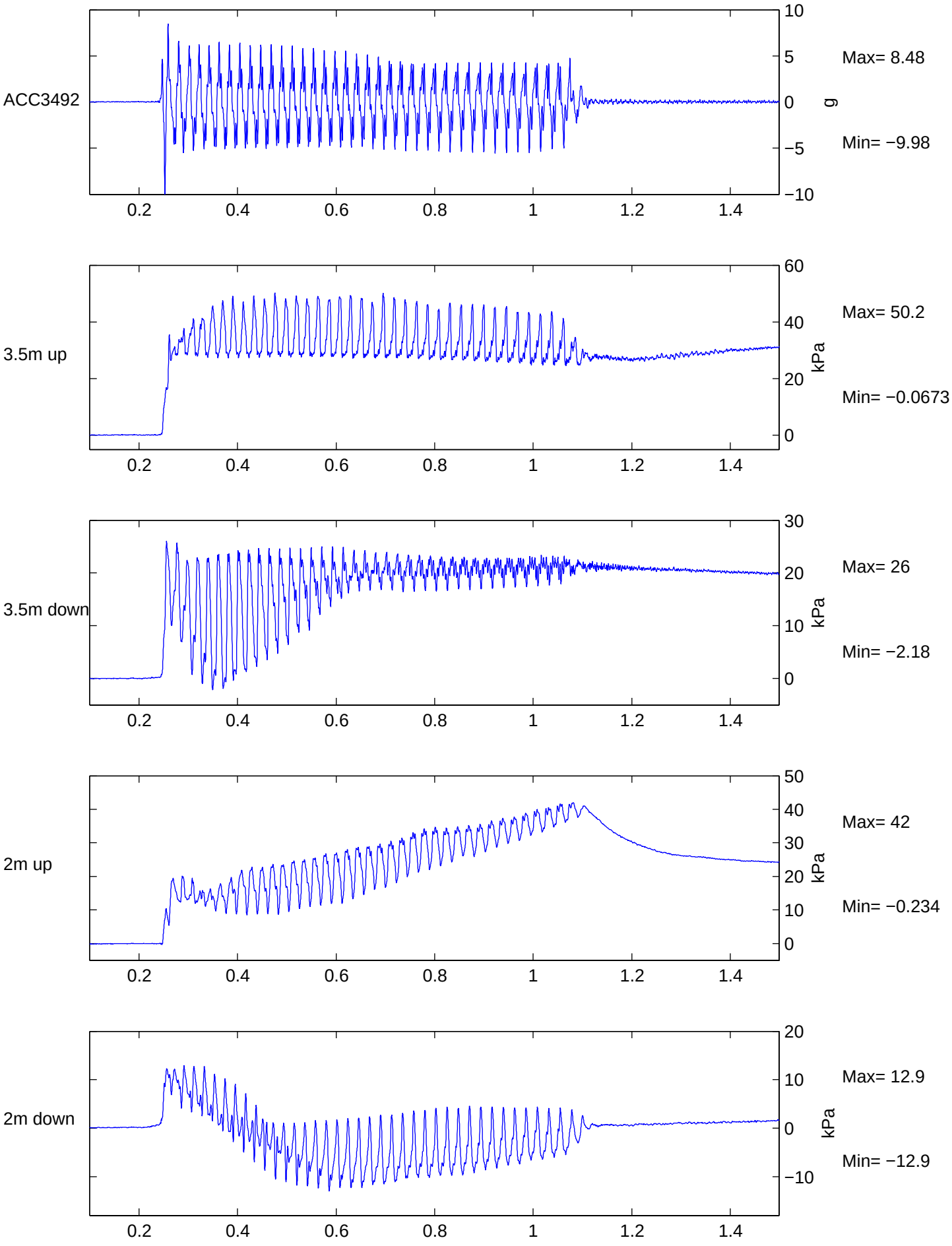

TEST SKH−17 FLIGHT 1		Scales: Model 8th order Butterworth Filter at 500Hz Short−Term Time Records	Earthquake 1	Figure No. 23

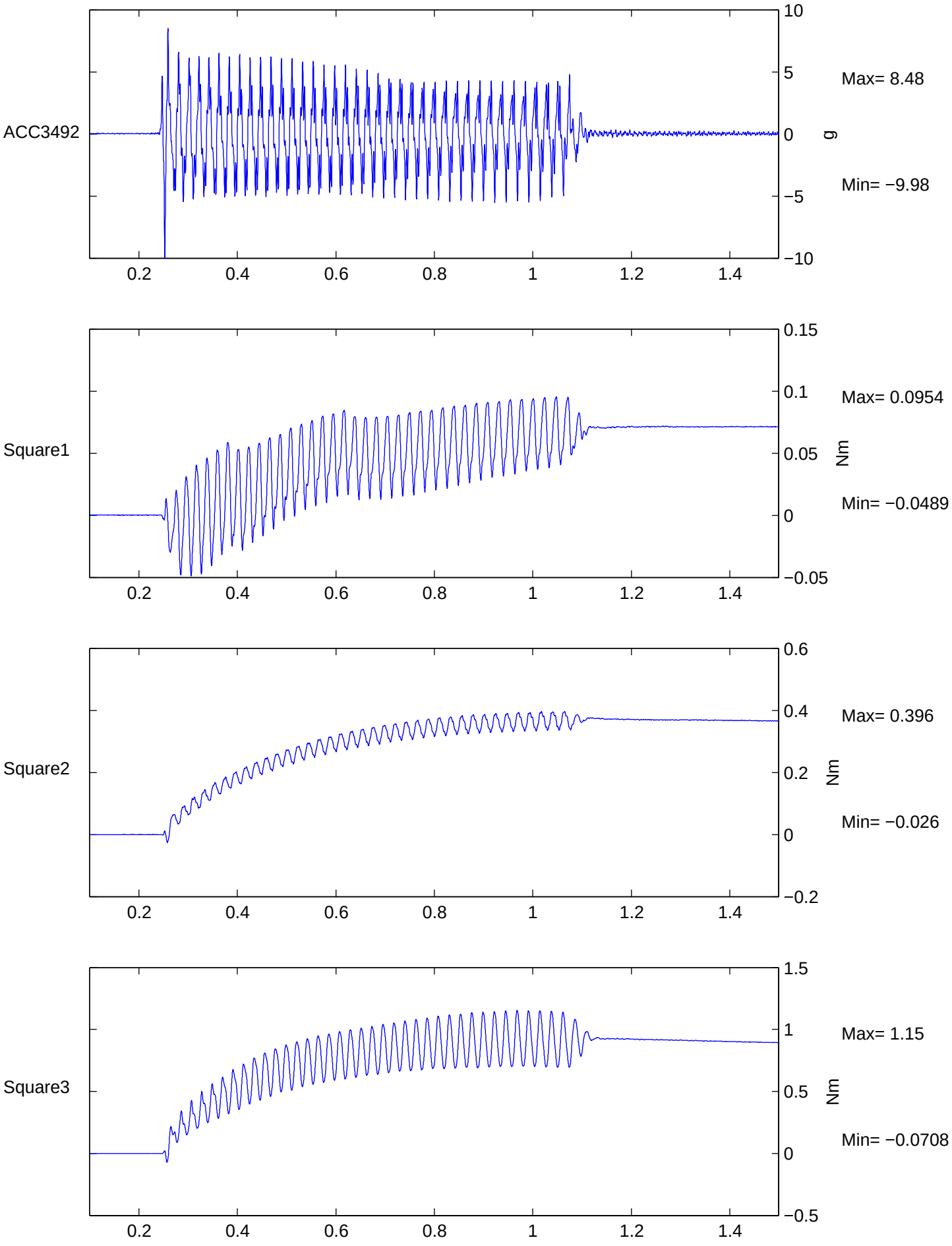

TEST SKH−17 FLIGHT 1		Scales: Model 8th order Butterworth Filter at 500Hz Short−Term Time Records	Earthquake 1	Figure No. 24a

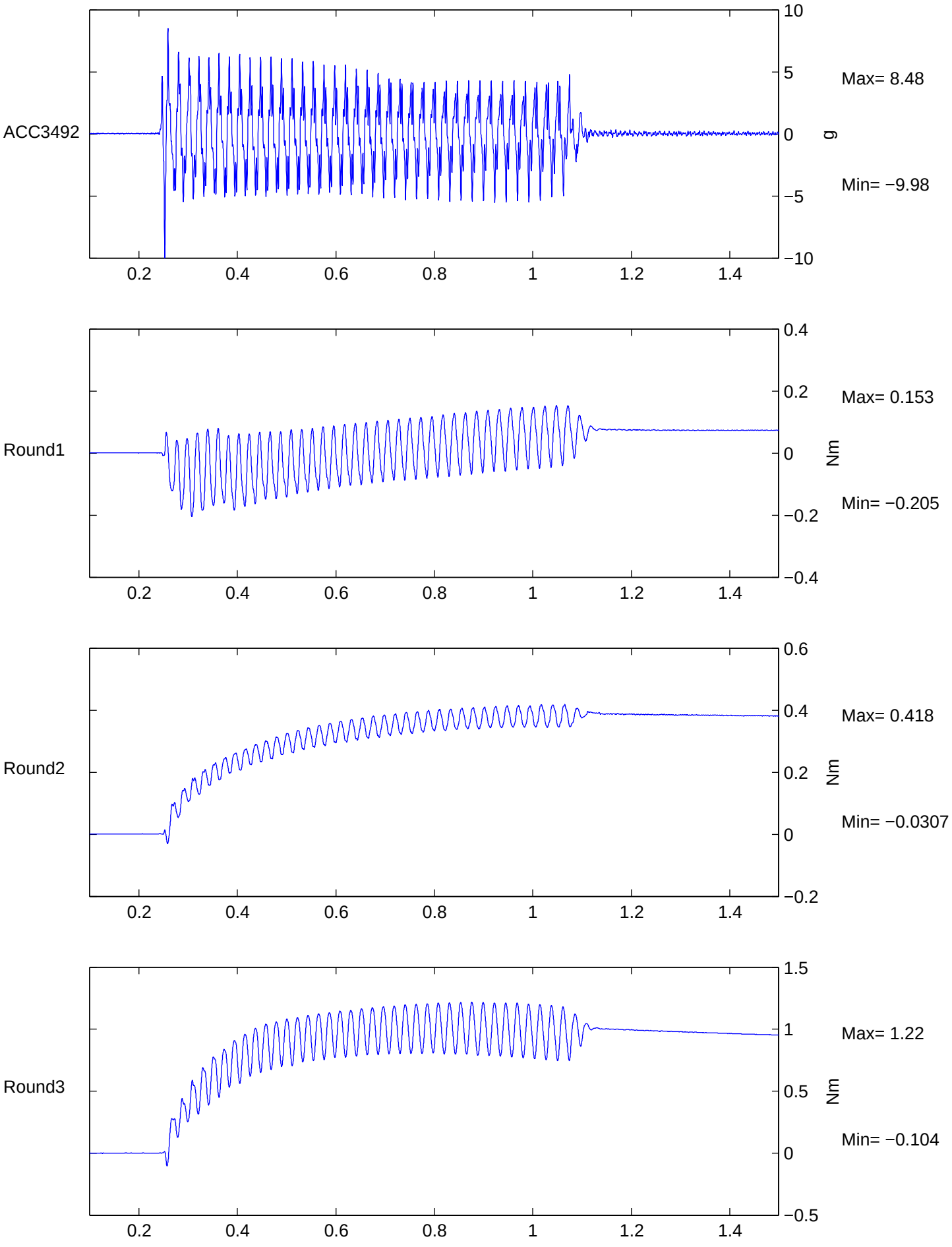

TEST SKH−17 FLIGHT 1		Scales: Model 8th order Butterworth Filter at 500Hz Short−Term Time Records	Earthquake 1	Figure No. 24b

5. Conclusions

It has been shown that centrifuge modelling can be used to investigate the dynamic behaviour of liquefying slopes and their interaction with pile foundations. It has also been shown that significant lateral loads can be imposed on these pile foundations and that near-pile soil dilation plays an important part in this behaviour.

6. Acknowledgements

The author would like to acknowledge the financial contributions of Shimizu Corporation, Japan, and of the Engineering and Physical Sciences Research Council to this work. The author would also like to acknowledge the contribution of Dr Gopal Madabhushi to this research.

7. References

Haigh, S.K., Madabhushi, S.P.G., Soga, K., Taji, Y. & Shamoto, Y. (2000) "Lateral spreading during centrifuge model earthquakes", Proc. GeoEng2000, Melbourne, Australia

Haigh, S.K. (2002), "Effects of liquefaction-induced lateral spreading on pile foundations in sloping ground", PhD Thesis, Cambridge University, UK

Hamada, M. (1992), "Large ground deformations and their effects on lifelines: 1964 Niigata earthquake", in Case Studies of Liquefaction and Lifeline Performance During Past Earthquakes, Hamada & O'Rourke eds., Technical Report NCEER-92-0001, NCEER, Buffalo, NY

Lee, S.Y. (1990), "Centrifuge modelling of cone penetration testing in cohesionless soils", PhD Thesis, Cambridge University, UK

Tan, F.S.C. (1990), "Centrifuge and theoretical modelling of conical footings on sand", PhD Thesis, Cambridge University, UK